



# The Black Hole in the Most Massive Ultracompact Dwarf Galaxy M59-UCD3

Christopher P. Ahn<sup>1</sup>, Anil C. Seth<sup>1</sup>, Michele Cappellari<sup>2</sup>, Davor Krajnović<sup>3</sup>, Jay Strader<sup>4</sup>, Karina T. Voggel<sup>1</sup>, Jonelle L. Walsh<sup>5</sup>, Arash Bahramian<sup>4</sup>, Holger Baumgardt<sup>6</sup>, Jean Brodie<sup>7,8</sup>, Igor Chilingarian<sup>9,10</sup>, Laura Chomiuk<sup>4</sup>, Mark den Brok<sup>3</sup>, Matthias Frank<sup>11</sup>, Michael Hilker<sup>12</sup>, Richard M. McDermid<sup>13,14,15</sup>, Steffen Mieske<sup>16</sup>, Nadine Neumayer<sup>17</sup>, Dieu D. Nguyen<sup>1</sup>, Renuka Pechetti<sup>1</sup>, Aaron J. Romanowsky<sup>7,18</sup>, and Lee Spitler<sup>13,14,15</sup>

<sup>1</sup> University of Utah, Department of Physics & Astronomy, 115 S 1400 E, Salt Lake City, UT 84105, USA; [chris.ahn43@gmail.com](mailto:chris.ahn43@gmail.com)

<sup>2</sup> Sub-department of Astrophysics, Department of Physics, University of Oxford, Denys Wilkinson Building, Keble Road, Oxford, OX1 3RH, UK

<sup>3</sup> Leibniz-Institut für Astrophysik Potsdam (AIP), An der Sternwarte 16, D-14482 Potsdam, Germany

<sup>4</sup> Michigan State University, USA

<sup>5</sup> George P. and Cynthia Woods Mitchell Institute for Fundamental Physics and Astronomy, Department of Physics and Astronomy, Texas A&M University, College Station, TX 77843, USA

<sup>6</sup> University of Queensland, Australia

<sup>7</sup> University of California Observatories, 1156 High Street, Santa Cruz, CA 95064, USA

<sup>8</sup> University of California, Santa Cruz, USA

<sup>9</sup> Smithsonian Astrophysical Observatory, 60 Garden St., MS09, Cambridge, MA 02138, USA

<sup>10</sup> Sternberg Astronomical Institute, M.V. Lomonosov Moscow State University, 13 Universitetsky Prospect, 119992 Moscow, Russia

<sup>11</sup> Landessternwarte, Zentrum für Astronomie der Universität Heidelberg, Königsstuhl 12, D-69117 Heidelberg, Germany

<sup>12</sup> European Southern Observatory, Garching, Germany

<sup>13</sup> Australian Astronomical Observatory, P.O. Box 915, North Ryde NSW 1670, Australia

<sup>14</sup> Research Centre for Astronomy, Astrophysics & Astrophotonics, Macquarie University, Sydney, NSW 2109, Australia

<sup>15</sup> Department of Physics & Astronomy, Macquarie University, Sydney, NSW 2109, Australia

<sup>16</sup> European Southern Observatory Alonso de Cordova 3107, Vitacura, Chile

<sup>17</sup> Max-Planck-Institut für Astronomie, Germany

<sup>18</sup> Department of Physics & Astronomy, San José State University, One Washington Square, San Jose, CA 95192, USA

Received 2018 March 21; revised 2018 April 3; accepted 2018 April 4; published 2018 May 11

## Abstract

We examine the internal properties of the most massive ultracompact dwarf galaxy (UCD), M59-UCD3, by combining adaptive-optics-assisted near-IR integral field spectroscopy from Gemini/NIFS and *Hubble Space Telescope* (*HST*) imaging. We use the multiband *HST* imaging to create a mass model that suggests and accounts for the presence of multiple stellar populations and structural components. We combine these mass models with kinematics measurements from Gemini/NIFS to find a best-fit stellar mass-to-light ratio ( $M/L$ ) and black hole (BH) mass using Jeans anisotropic models (JAMs), axisymmetric Schwarzschild models, and triaxial Schwarzschild models. The best-fit parameters in the JAM and axisymmetric Schwarzschild models have BHs between 2.5 and 5.9 million solar masses. The triaxial Schwarzschild models point toward a similar BH mass but show a minimum  $\chi^2$  at a BH mass of  $\sim 0$ . Models with a BH in all three techniques provide better fits to the central  $V_{\text{rms}}$  profiles, and thus we estimate the BH mass to be  $4.2_{-1.7}^{+2.1} \times 10^6 M_{\odot}$  (estimated  $1\sigma$  uncertainties). We also present deep radio imaging of M59-UCD3 and two other UCDs in Virgo with dynamical BH mass measurements, and we compare these to X-ray measurements to check for consistency with the fundamental plane of BH accretion. We detect faint radio emission in M59cO but find only upper limits for M60-UCD1 and M59-UCD3 despite X-ray detections in both these sources. The BH mass and nuclear light profile of M59-UCD3 suggest that it is the tidally stripped remnant of a  $\sim 10^9$ – $10^{10} M_{\odot}$  galaxy.

**Key words:** galaxies: clusters: general – galaxies: dwarf – galaxies: evolution – galaxies: formation – galaxies: kinematics and dynamics

**Supporting material:** tar.gz files

## 1. Introduction

The past few decades have seen the emergence of compact stellar systems that have blurred the conventional lines, based on properties such as mass, luminosity, and size, between star clusters and galaxies (Hilker et al. 1999; Drinkwater et al. 2000). One such classification of objects, the ultracompact dwarf galaxies (UCDs), occupies the region between globular clusters (GCs) and compact ellipticals (cEs) (e.g., Brodie et al. 2011; Misgeld & Hilker 2011; Pfeffer & Baumgardt 2013; Norris et al. 2014; Janz et al. 2016). With masses and radii of  $M > 2 \times 10^6 M_{\odot}$  and  $r > 10$  pc, UCDs are among the densest stellar systems in the universe. However, the nature and origin of these dense objects are still widely

debated. Early interpretations suggested that UCDs could be the most massive GCs (e.g., Fellhauer & Kroupa 2002, 2005; Mieske et al. 2002; Kissler-Patig et al. 2006; Murray 2009) or possibly the tidally stripped remnants of dwarf galaxies (Bekki et al. 2001, 2003; Drinkwater et al. 2003; Pfeffer & Baumgardt 2013; Strader et al. 2013; Forbes et al. 2014). However, there is evidence that both formation mechanisms could contribute to the UCD population we observe (Brodie et al. 2011; Da Rocha et al. 2011; Norris & Kannappan 2011; Janz et al. 2016).

In the past decade, observational results based on structural information from *Hubble Space Telescope* (*HST*) imaging combined with integrated velocity dispersion measurements have shown an interesting trend: UCDs' dynamical mass-to-light ratios ( $M/L_{\text{dyn}}$ ) appear to be systematically elevated when compared to

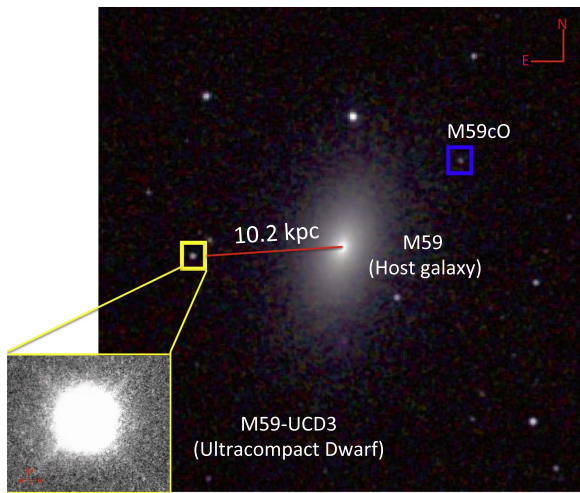


**Figure 1.** M59/M59-UCD3 system discussed in this paper. Here the main image shows the Two Micron All Sky Survey Large Galaxy Atlas image (Jarrett et al. 2003). M59-UCD3 is outlined in the yellow box. The inset image is a zoom-in *HST* image taken through the F814W filter on the WFC3 instrument. We also outline another UCD in this system, M59cO, in blue. The red line connecting the UCD to the host galaxy shows the projected distance assuming that M59-UCD3 is at a distance of 16.5 Mpc.

the canonical stellar population estimates (Haşegan et al. 2005; Dabringhausen et al. 2008; Mieske et al. 2008; Taylor et al. 2010; Frank et al. 2011; Strader et al. 2013). These results prompted suggestions of variations in the stellar initial mass function (IMF) of UCDs (top-heavy: Murray 2009; Dabringhausen et al. 2009, 2010; bottom-heavy: Mieske & Kroupa 2008). Further explanations have suggested that these elevated  $M/L$ s could be explained by ongoing tidal stripping (Forbes et al. 2014; Janz et al. 2016), or, as a relic of a massive progenitor galaxy in the tidal stripping scenario, a central massive black hole (BH) making up  $\sim 10\%$ – $15\%$  of the total mass (Mieske et al. 2013). Supermassive black holes (SMBHs) have been confirmed in four UCDs with masses  $M > 10^7 M_\odot$ ; three in the Virgo Cluster (Seth et al. 2014; Ahn et al. 2017), and one in the Fornax Cluster (Afanasyev et al. 2018). A search for SMBHs in two lower-mass ( $M < 10^7 M_\odot$ ) UCDs in Centaurus A yielded a nondetection (Voggel et al. 2018). However, Voggel et al. (2018) also showed that the dynamical-to-stellar  $M/L$ s were overestimated in previous studies. The combination of this evidence still supports the idea that most UCDs with apparently high dynamical-to-stellar mass ratios (including a vast majority of UCDs above  $10^7 M_\odot$ ) host SMBHs. Lower-mass UCDs may be the high-mass end of the GC distribution. This view would be consistent with the analysis of the stripped nuclei contribution to UCDs in  $\Lambda$ CDM simulations by Pfeffer et al. (2014, 2016).

Despite the fact that all of the detected SMBHs are found in massive ( $M > 10^7 M_\odot$ ) UCDs, the most massive UCD discovered to date, M59-UCD3 ( $M_* \sim 2 \times 10^8 M_\odot$ ,  $r_e \sim 25$  pc), has been left out. This is in part due to its recent discovery (Liu et al. 2015; Sandoval et al. 2015) and the lack of high-resolution imaging data needed for dynamical modeling. Thus, M59-UCD3 serves as an important test of the idea that the most massive UCDs host SMBHs. In this paper we present the dynamical modeling techniques and results for M59-UCD3.

An image of M59-UCD3 and its host galaxy (M59 = NGC 4621) is shown in Figure 1. M59-UCD3 is located 10.2 kpc in projection from the center of M59, assuming an average distance of 16.5 Mpc to the Virgo Cluster based on surface brightness fluctuations (Mei et al. 2007). We note that

the individual distance of M59 has been measured to be  $14.9 \pm 0.4$  Mpc (Mei et al. 2007), and this distance has been used in previous luminosity and mass estimates; our assumed 16.5 Mpc will yield a 10% higher dynamical mass estimate relative to the previous mass determination (Liu et al. 2015), while at 16.5 Mpc M59-UCD3 has a measured  $M_V = -14.8$  (Sandoval et al. 2015). We adopt the conventional definition of  $\Gamma \equiv (M/L)_{\text{dyn}}/(M/L)_*$ , which is the ratio between the dynamically determined total  $M/L$  and the stellar  $M/L$  inferred from stellar population modeling. Throughout this paper, we assume a Chabrier IMF for the stellar population models. The metallicity of M59-UCD3 has been estimated to be near solar, with  $[\text{Fe}/\text{H}] \sim -0.01$  and  $[\alpha/\text{Fe}] \sim 0.21$  (Liu et al. 2015; Sandoval et al. 2015; Janz et al. 2016; Villaume et al. 2017). These values of near solar metallicity and moderate alpha-element enhancement are consistent with previously measured high-mass UCDs (Evstigneeva et al. 2007; Chilingarian & Mamon 2008; Firth et al. 2009; Francis et al. 2012; Strader et al. 2013; Janz et al. 2016). All magnitudes are reported in the AB magnitude system. Furthermore, all magnitudes and colors have been extinction corrected using  $A_{F475W} = 0.100$  and  $A_{F814W} = 0.052$  (Schlafly & Finkbeiner 2011).

This paper is organized as follows: Section 2 discusses the data used for analysis, how we determined a density profile, and how the kinematics were modeled. In Section 3 we present our three dynamical modeling techniques and the results from each. Section 4 discusses the radio/X-ray observations of UCDs and whether these observations can be used to infer the presence or not of an accreting SMBH. In Section 5 we discuss the implications of the results and present our conclusions.

## 2. Data and Methods

In this section we present the data and our reduction techniques. Section 2.1 discusses the *HST* images and our methods for deriving a mass model. Section 2.2 explains the reduction of our Gemini/NIFS integral field spectroscopy and the derivation of the kinematics.

### 2.1. Imaging Data and Deriving a Mass Model

We obtained images of M59-UCD3 from the *HST* GO Cycle 23 program 14067 (PI: Ahn) with the Wide Field Camera 3 (WFC3) instrument, which has a pixel scale of  $0''.04 \text{ pixel}^{-1}$ . Our data were taken through the F475W and F814W filters. The exposure times in each filter were 1470 and 747 s for F475W and F814W, respectively.

We derived a point-spread function (PSF) for each filter following the procedure outlined in previous studies (Evstigneeva et al. 2007; Ahn et al. 2017). To briefly summarize, we generated the distorted PSF with TinyTim and placed these PSFs in an empty copy of the raw *HST* flat-fielded image at the location of our observed target. The distorted PSFs were then passed through MultiDrizzle using the same parameters as were used for the data. This produces model PSFs that are processed in the same way as the original data.

The background (sky) level is traditionally determined from empty portions of the image. However, UCDs generally fall within the stellar halo of their host galaxy. Therefore, the sky level is not uniform across the image. To account for this, we added the MultiDrizzle level, subtracted by the *HST* reduction pipeline, back in and modeled the sky as a tilted plane. This

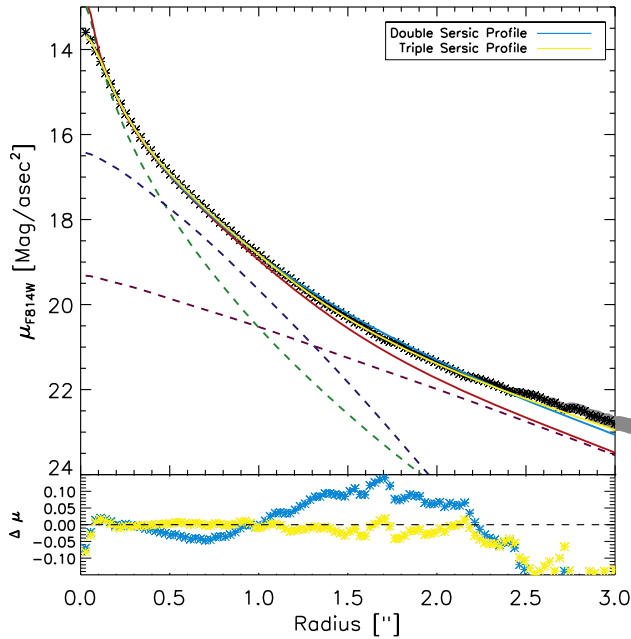


**Figure 2.** Surface brightness profile of M59-UCD3 in *HST*/F814W, which was used for dynamical modeling. Black stars are data, cyan lines are convolved double-component Sérsic profile models, yellow lines are convolved triple-component Sérsic profile models, the red line is the triple-component Sérsic reconstructed profile, and green, blue, and purple lines are the individual Sérsic components. The gray bands represent the uncertainty in our background sky determination. The residuals between the data and convolved models are shown in the bottom panel.

was accomplished by masking all foreground/background objects, including our UCD, in the image. The good pixels (determined from the DQ extension of the image) were then weighted by their corresponding errors. Finally, a plane was fitted to the image to represent the sky level. The formal uncertainties on the sky level determination in this method are negligible. However, a clear systematic effect is seen in that the mean value of the data minus sky model is offset from zero. We regard this as indicative of the systematic uncertainties, which are 0.86 counts in F475W and 1.38 counts in F814W. We use these uncertainties for plotting purposes only in the surface brightness profile (in Figure 2 as gray bands) and color profile (in Figure 3 as our error bars on the data).

To enable dynamical modeling of M59-UCD3, we needed to create a model to represent the luminosity and mass distribution. Typically, in compact objects such as UCDs, the mass is assumed to trace the light (e.g., Mieske et al. 2013; Seth et al. 2014). However, previous studies have found significant color gradients in UCDs, suggesting multiple stellar populations (Chilingarian & Mamon 2008; Evstigneeva et al. 2008; Ahn et al. 2017). Therefore, two-filter data are essential for determining the most accurate luminosity and mass profiles of UCDs. The uncertainties in the luminosity and mass profile combinations are discussed in Section 3.1. For now, we discuss the general procedure for determining our luminosity and mass distributions.

The surface brightness profile was determined by fitting the data in each filter to a PSF-convolved, multiple-component Sérsic profile using the two-dimensional fitting algorithm, GALFIT (Peng et al. 2002). The parameters of the individual Sérsic profiles that were fitted include the total magnitude

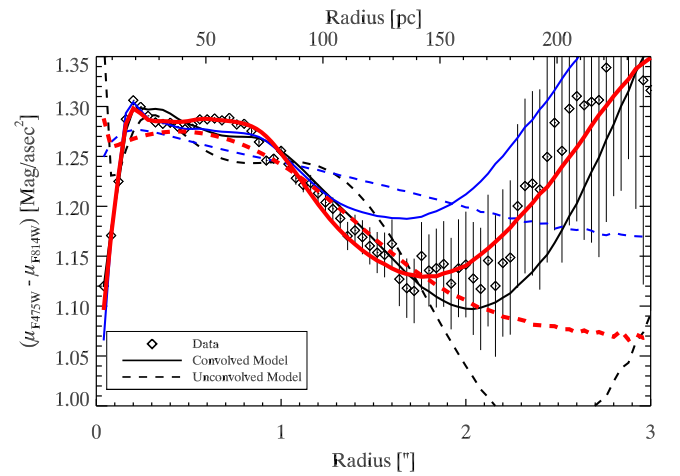


**Figure 3.** Color profile of M59-UCD3 shown as black diamonds. The error bars are calculated from the uncertainty in our background (sky) level determinations. The solid lines indicate the triple-component Sérsic model fits that have been convolved with the *HST* PSF. Dashed lines show models that are unconvolved. The colors represent whether the shape parameters of the Sérsic profiles were independent (black) or fixed (red and blue). Blue lines indicate that the shape parameters of the F475W filter were held fixed to the best-fit F814W Sérsic models, and red lines are vice versa. The unconvolved fixed models (red and blue) provide a well-defined color for each Sérsic component. Our default model is shown in red. Here the inner, middle, and outer colors are 1.26, 1.32, and 1.06 mag for our default model, respectively. See Section 2.1 for a discussion on our choice of the default model.

( $m_{\text{tot}}$ ), effective radius ( $R_e$ ), Sérsic exponent ( $n$ ), position angle (PA), and axis ratio ( $q$ ). The fitting was done in two ways, similar to our previous study (Ahn et al. 2017). In short, we fitted while allowing all of the above parameters to vary, henceforth referred to as the “free” fit. The initial fits showed an isophotal twist between the individual Sérsic profiles. However, the axis ratios of the outer profiles were nearly circular ( $q \sim 0.99$ ). Furthermore, two of the three dynamical modeling techniques are restricted to axisymmetric potentials and thus do not allow for isophotal twists. To enable comparison between all three techniques, we fixed the axis ratio of the outer profiles to be perfectly circular and fitted the data again. Next, we fitted the data while fixing  $R_e$ ,  $n$ , PA, and  $q$  to the best-fit model from the other filter, which we call the “fixed” fit. For example, the fixed F814W fit contains all of the shape parameters from the best-fit F475W model, where only the total magnitude is varied. Since the only free parameter is the total magnitude, these fits provide a well-defined color for each Sérsic profile. The Sérsic profiles used to create the default luminosity and mass models are shown in Figure 2, and the parameters of the best-fit models are shown in Table 1. We chose the default model to be the fixed F814W fit (outlined in bold in Table 1) because (1) of its ability to accurately reproduce the surface brightness profile, (2) it clearly provides the best fit to the color profile (discussed below), and (3) it provides a well-defined color for each Sérsic component. However, as discussed in Section 3.1, the choice of the luminosity and mass model produces a minor effect on the results of the dynamical models.

The most massive ( $M > 10^7 M_\odot$ ) UCDs have been found to consist of two components: a dense central component, and a more diffuse extended component, as shown by the two-component profile fits in previous studies (Evstigneeva et al. 2007, 2008; Chilingarian & Mamon 2008; Strader et al. 2013; Ahn et al. 2017; Voggel et al. 2018; Afanasiev et al. 2018). Shown in cyan in Figure 2, a two-component Sérsic profile



**Table 1**  
Best-fit Sérsic Parameters

Component	Parameter	F475W	F814W
	$\chi^2$	1.045	1.356
Inner	$m_{\text{tot}}$	<b>17.27</b>	16.24
	$m_{\text{tot}}$ fixed <sup>a</sup>	17.58	<b>16.01</b>
	$R_e$ (arcsec)	<b>0.21</b>	0.26
	$R_e$ (pc)	<b>16.8</b>	20.8
	$n$	<b>2.04</b>	1.72
	$q$	<b>0.74</b>	0.73
	PA (deg) <sup>2</sup>	<b>-6.41</b>	-6.36
Middle	$m_{\text{tot}}$	<b>18.02</b>	16.70
	$m_{\text{tot}}$ fixed <sup>a</sup>	17.86	<b>16.70</b>
	$R_e$ (arcsec)	<b>0.50</b>	0.35
	$R_e$ (pc)	<b>40.0</b>	28.0
	$n$	<b>0.80</b>	5.23
	$q$	<b>1.00</b>	1.00
Outer	$m_{\text{tot}}$	<b>18.84</b>	16.95
	$m_{\text{tot}}$ fixed <sup>a</sup>	18.20	<b>17.78</b>
	$R_e$ (arcsec)	<b>1.24</b>	0.56
	$R_e$ (pc)	<b>99.2</b>	44.8
	$n$	<b>0.90</b>	0.90
	$q$	<b>1.00</b>	1.00

**Note.** The PA orientation is N = 0° and E = 90°. The default model (in bold) was constructed by fitting F475W first, allowing all parameters to be free. Then the shape parameters from the previous fit were held fixed and only  $m_{\text{tot}}$  is fit for F814W. Next, we tested fitting F814W first, allowing all parameters to be free. Then, the shape parameters from the previous fit were fixed and only  $m_{\text{tot}}$  for F475W is fit. The numbers from the second approach are not bolded.

<sup>a</sup> The “fixed” magnitudes show the total magnitude when the shape parameters of the Sérsic profiles are held fixed to the other filter.

provides a suitable fit to the data within the central 2''.5. However, a much better fit out to 3'' was obtained by allowing a three-component Sérsic profile, shown in Figure 2 as yellow. The outer component is rounder and, as we will see below, appears to be bluer than the inner components. The inner Sérsic components can also be replaced by a single King profile; a two-component King + Sérsic profile provides an equally suitable fit as the three-component Sérsic out to 3''. The central King model component in this fit has a core radius  $R_c = 0''.05$  (4 pc) and a concentration parameter  $c = 1.42$ . We stick with our three-component Sérsic model fit for the remainder of the paper because of the ease of transforming this model into our mass models.

The simulations of Pfeffer & Baumgardt (2013) show that when galaxies are stripped into UCDs, they show a two-component structure, with the inner component consisting of the galaxies' nuclear star cluster (NSC) surrounded by the remains of the tidally stripped galaxy. Therefore, the multiple-component model that is required to fit the surface brightness profile (regardless of the model choice) provides evidence that M59-UCD3 is likely a tidally stripped remnant.

The total luminosity in each band (within the central 3'') and effective radius calculated from the unconvolved Sérsic profiles are found to be  $L_{\text{F814W}} = (1.18\text{--}1.19) \times 10^8 L_{\odot}$ ,  $L_{\text{F475W}} = (6.1\text{--}6.2) \times 10^7 L_{\odot}$ , and  $R_e = 26\text{--}29$  pc or  $0''.32\text{--}0''.36$ , respectively. Here the ranges are quoted based on the total luminosity and effective radius calculated across all free and fixed models. Our effective radii are consistent with previous measurements. However, our calculated luminosity is slightly lower than the

previously estimated  $L_g = 9.5 \times 10^7 L_{\odot}$  (Liu et al. 2015; Sandoval et al. 2015). We attribute these deviations in the luminosity to our deeper *HST* imaging data, where previous studies were limited to ground-based data only. Each of the best-fit Sérsic profiles was then parameterized by a multi-Gaussian expansion (MGE; Emsellem et al. 1994; Cappellari 2002), using the MGE\_FIT\_1D fitting method and code<sup>19</sup> of Cappellari (2002) for use in the dynamical modeling.

Creating dynamical models that reproduce the observed kinematics requires a luminosity and mass profile. To determine the mass profile, we make use of our dual-filter *HST* data to test for the presence of stellar population variations. M59-UCD3 shows a complicated color profile that varies by 0.25 mag within the central 3'', as shown in Figure 3. Here the diamonds represent the data, where the error bars are calculated from our estimated systematic background effects, discussed above. Solid lines represent the convolved model, and dashed lines represent the unconvolved model. The colored lines show whether the parameters of the Sérsic fits were independent (black) or fixed (blue and red). Blue lines indicate that the shape parameters from the F475W filter were held fixed to the F814W filter, and red lines are vice versa. It is clear, from the unconvolved models, that the bluest colors near the center are due to PSF effects and there is a gradient toward bluer colors at larger radii. This is unique when compared to other UCDs, which generally show either no overall trend or a gradient toward redder colors at larger radii (Chilingarian & Mamon 2008; Evstigneeva et al. 2008; Seth et al. 2014; Janz et al. 2015; Ahn et al. 2017).

The unconvolved fixed models (dashed blue and red lines in Figure 3) provide a well-defined color for the three Sérsic components. However, the fixed F814W Sérsic shape parameters (red lines) provide a better fit to the color profile, which motivated our choice of the default model. Here the inner-component color is F475W–F814W = 1.26, the middle-component color is F475W–F814W = 1.32, and the outer-component color is F475W–F814W = 1.06. We used these colors along with the Bruzual & Charlot (2003) Padova 1994 simple stellar population (SSP) models and corresponding code,<sup>20</sup> assuming solar metallicity and a Chabrier IMF, to determine the mass-to-light ratio ( $M/L$ ). The default Bruzual & Charlot (2003) color tables and corresponding  $M/L$ s do not include our *HST* filter set. Therefore, we downloaded the filter transmission curves and reran the composite stellar population model code. We found the inner, middle, and outer  $M/L_{\text{F814W,*}}$  to be  $2.5 \pm 0.4$ ,  $2.9 \pm 0.4$ , and  $1.0 \pm 0.1$ , with corresponding ages of 9.9, 13.7, and 2.8 Gyr, respectively. Here the error bars are calculated assuming an uncertainty of  $\pm 0.05$  mag in our color determinations. We also determined the total mass by multiplying the total luminosity by the corresponding  $M/L$  for each Sérsic component. We found the inner-component, middle-component, and outer-component total stellar mass to be  $(17.3 \pm 2.8) \times 10^7 M_{\odot}$ ,  $(10.6 \pm 1.5) \times 10^7 M_{\odot}$ , and  $(1.2 \pm 0.1) \times 10^7 M_{\odot}$ , respectively. The mass density profile was then determined by multiplying the luminosity model MGEs by their corresponding  $M/L$ s. We note that to test the systematic effects of our choice of the default mass profile, we also determined two additional mass density profiles by (1) computing the  $M/L$  from the color of the free Sérsic profile fits (black lines in Figure 3) at the FWHM of each Gaussian

<sup>19</sup> <http://purl.org/cappellari/software>

<sup>20</sup> <http://software.astrogrid.org/p/cea/latest/cec/config/galaxev/GALAXEV.html>

**Table 2**

Default Multi-Gaussian Expansion Used in the Dynamical Modeling

Mass ( $M_{\odot} \text{ pc}^{-2}$ ) <sup>a</sup>	$I_K$ ( $L_{\odot} \text{ pc}^{-2}$ ) <sup>b</sup>	$\sigma$ (arcsec)	$q$
294397.	304328.	0.001	0.74
361060.	373239.	0.004	0.74
370914.	383426.	0.011	0.74
308330.	318732.	0.027	0.74
199887.	206630.	0.059	0.74
99196.3	102542.	0.115	0.74
36071.5	37288.3	0.209	0.74
9451.14	9769.96	0.356	0.74
1737.86	1796.49	0.576	0.74
210.794	217.905	0.903	0.74
11.8194	12.2182	1.459	0.74
<hr/>			
2547.19	2355.68	0.055	1.00
6801.10	6289.76	0.180	1.00
8380.02	7749.98	0.355	1.00
3882.25	3590.37	0.541	1.00
427.301	395.175	0.738	1.00
<hr/>			
44.2053	101.759	0.073	1.00
116.224	267.543	0.263	1.00
173.015	398.277	0.601	1.00
128.835	296.574	1.050	1.00
40.5159	93.2663	1.566	1.00
3.46218	7.96984	2.175	1.00

**Notes.** The PA adopted for all of the dynamical models was  $-6^{\circ}41'$ , where  $N = 0^{\circ}$  and  $E = 90^{\circ}$ . The horizontal lines separate the individual Sérsic models.

<sup>a</sup> The  $M/L$  was used to determine the mass profiles. These methods are described in Section 2.1.

<sup>b</sup> The luminosity MGEs were created in the  $K$  band, which required an assumption on the absolute magnitude of the Sun. We assumed these values to be 4.523 in F814W and 3.29 in  $K$  taken from <http://www.baryons.org/ezgal/filters.php>. See Section 2.1 for a more detailed explanation of how the luminosity profile was derived.

component in the MGE luminosity profile and (2) assuming a mass-follows-light model, which is equivalent to creating a mass density profile where all of the Sérsic components have been scaled by the flux-weighted  $M/L$  described below. The latter test was motivated by the bluer outermost component, which could also be interpreted as a metal-poor old stellar population. As discussed in Section 3.1, this results in an  $M/L_{F814W,*} = 1.9$ , which is intermediate to our mass-follows-light model.

The luminosity is used to calculate the center of each kinematic bin and create the observed kinematic field. Since our kinematic data were taken in the  $K$  band, we determined a luminosity MGE in that band using the color profiles and SSPs. This was accomplished by creating a color-color diagram of F814W- $K$  versus F475W-F814W from the SSP models. We then used our derived color to infer the F814W- $K$  color. For each Sérsic component we found these colors to be F814W- $K = 2.28, 2.32,$  and  $2.12$  for the inner, middle, and outer components, respectively. These colors lead to a scale factor in the luminosity surface density for each component of 2.59 (inner), 2.69 (middle), and 2.24 (outer). These scale factors were multiplied by the luminosity profile for each component to make our  $K$ -band MGEs used in the dynamical models. The best-fit model MGE, for our default model, is shown in Table 2.

Finally, the SSP models and color profiles were used to determine a flux-weighted average  $M/L$ . We computed this by

determining the flux within the central  $3''$  from model images of the inner, middle, and outer Sérsic profiles and then weighting the individual  $M/L$ s calculated above by their corresponding flux. We found the average  $M/L_{F814W,*}$  to be  $2.47 \pm 0.25$  (assuming  $\sim 10\%$  uncertainties similar to individual  $M/L$ s). We calculated the overall F475W-F814W color to be 1.26. Using the SSP models, described above, we estimate  $V - F814W = 0.86$  (Bruzual & Charlot 2003). This corresponds to  $M/L_{V,*} = 4.2 \pm 0.4$ , which is consistent with previous results (Liu et al. 2015). We note that the Mieske et al. (2013) Equation (4) estimate of  $M/L_{V,*}$  for  $[\text{Fe}/\text{H}] = -0.01$  is 4.07 based on the mean between the Bruzual & Charlot (2003) and Maraston (2005) model predictions.

## 2.2. Kinematic Derivation

Our spectroscopic data were obtained with the Near-infrared Integral Field Spectrometer (NIFS) mounted on the Gemini North telescope using *Altair* laser guide star adaptive optics (Herriot et al. 2000; McGregor et al. 2003; Boccas et al. 2006). The observations were taken on the nights of 2015 May 4, 5, and 6 in the  $K$  band at wavelengths from 2.0 to  $2.4 \mu\text{m}$ . Gemini/NIFS data are taken in  $0''.1 \times 0''.04$  pixels over a  $3''$  field of view with a spectral resolution of  $\lambda/\delta\lambda \sim 5700$  ( $\sigma_{\text{inst}} = 22 \text{ km s}^{-1}$ ).

Our data were reduced following the same procedure as in our previous studies, using the Gemini version 1.13 IRAF package (Seth et al. 2014; Ahn et al. 2017). To summarize, first, arc lamp and Ronchi mask images were used to determine the spatial and spectral geometry of the images. Next, the spectra were sky subtracted, were flat-fielded, had bad pixels removed, and were split into long-slit slices. Finally, the spectra were corrected for telluric absorption with an AOV telluric star taken on the same night using the NFTELLURIC procedure. The final data cube consisted of eight (five on May 4, one on May 5, and two on May 6) 900 s on-source exposures taken in either an object-sky-object or object-sky sequence. The object exposures were dithered to give independent sky measurements for each exposure and to improve the signal-to-noise ratio (S/N). We created our own version of NIFCUBE and NSCOMBINE to rebin the spectra to a  $0''.05 \times 0''.05$  pixel scale and enable error propagation of the variance spectrum. Finally, the spectra were combined using our IDL program, which centroids the nucleus and rejects bad pixels based on the nearest-neighboring pixels. The combined spectral data cube is available online.

The kinematic PSF was determined by convolving a Gauss +Moffat (1969) function with an *HST* model  $K$ -band image to match the surface brightness in the kinematic data cube. The *HST* model  $K$ -band image was derived following the same procedure outlined in Section 2.1, where we inferred the F814W- $K$  color using our derived color in each pixel combined with the SSP models. This model image was then convolved with a Gauss +Moffat function and fitted to the NIFS continuum image using the MPFIT2DFUN IDL code<sup>21</sup> (Markwardt 2009). We note that in order to quantify the systematic effects of our PSF determination on the dynamical models, we also convolved the *HST* model image with a double-Gaussian function. In this model PSF the central Gaussian contained 58% of the light with an FWHM of  $0''.201$  and the outer Gaussian contained 42% of the light with an FWHM of  $0''.894$ . Furthermore, we also determined a PSF where we fixed the central Gaussian FWHM in our Gauss

<sup>21</sup> <http://purl.com/net/mpfit>

+Moffat model to be the diffraction limit ( $\text{FWHM} = 0''.07$ ) of the NIFS instrument. In this diffraction-limited PSF the central Gaussian contained 24% of the light, while the Moffat function contained the remaining 76% with an FWHM of  $1''.08$ . The effects of these PSFs are discussed in Section 3.1. In our best-fit model function the central Gaussian was found to contain 35% of the light with an FWHM of  $0''.165$ . The Moffat function contained the remaining 65% of the light with an FWHM of  $1''.08$ . The one-dimensional analytic Gaussian+Moffat PSFs were again fitted by Gaussians using the MGE\_FIT\_1D procedure of Cappellari (2002).

The kinematics were measured by fitting the CO bandhead region ( $2.28\text{--}2.395\ \mu\text{m}$ ) to stellar templates using the IDL version of the penalized pixel algorithm pPXF, version 5.0.1 (see footnote 19; Cappellari & Emsellem 2004; Cappellari 2017). We convolved the high-resolution ( $\frac{\lambda}{\Delta\lambda} = 45,000$ ) Wallace & Hinkle (1996) stellar templates with the line-spread function (LSF), determined in each bin using sky exposures, before fitting. The bins were created using the Voronoi binning method and IDL code (see footnote 19) to achieve  $\text{S/N} = 25$  per resolution element (Cappellari & Copin 2003). However, beyond  $0''.5$  the bins were remade using sectors to further increase the S/N at the largest radii and to enable identification of rotation signatures. These outer bins have  $\text{S/N} \sim 20$ , with the outermost four bins having  $\text{S/N} \sim 12$ . We fit the radial velocity ( $V$ ), dispersion ( $\sigma$ ), skewness ( $h_3$ ), and kurtosis ( $h_4$ ) to the data. The uncertainties associated with the determined kinematics were estimated using a Monte Carlo simulation. Gaussian random noise was added to each spectral pixel in each bin, and the kinematics were fitted again. The standard deviations of the fits were taken as the  $1\sigma$  uncertainties. An example of the integrated ( $r < 0''.75$ ) kinematic fits is shown in Figure 4. The barycentric systemic velocity and integrated ( $r < 0''.75$ ) dispersion of M59-UCD3 were found to be  $434.5 \pm 0.6\ \text{km s}^{-1}$  and  $65.7 \pm 0.6\ \text{km s}^{-1}$ , respectively. Previous measurements of the radial velocity have ranged from  $373 \pm 18\ \text{km s}^{-1}$  to  $447 \pm 3\ \text{km s}^{-1}$  (Liu et al. 2015; Sandoval et al. 2015). Our measured radial velocity is within the range of previous measurements, but outside the quoted uncertainties. Our velocity dispersion is significantly lower than previous measurements, which have ranged from  $\sim 70\ \text{km s}^{-1}$  (no quoted uncertainty) to  $77.8 \pm 1.6\ \text{km s}^{-1}$  (Liu et al. 2015; Janz et al. 2016). We attempted to simulate the Liu et al. (2015) data by creating a Jeans anisotropic model (JAM) with the best-fit parameters (described below), a pixel size equivalent to their slit width, and seeing  $\text{FWHM} = 1''.85$ . Using these values, we found an integrated velocity dispersion of  $67\ \text{km s}^{-1}$ , which is still significantly lower than their measurement.

The kinematic maps for the four measured velocity moments are shown in Figure 5, and their corresponding values are shown in Table 3. The velocity map shows clear rotation, and  $h_3$  shows the common anticorrelation with the velocity. We also see a very definitive peak near the center of the dispersion map. The dispersion map has some significant asymmetries, with higher values at larger radii to the east of the nucleus.

Using kinematic fits<sup>22</sup> (Krajnović et al. 2006), we find that the rotation amplitude peaks at  $\sim 30\ \text{km s}^{-1}$  at a radius of  $0''.2$ . The  $V/\sigma$  reaches  $\sim 0.4$  at this radius and stays constant at larger

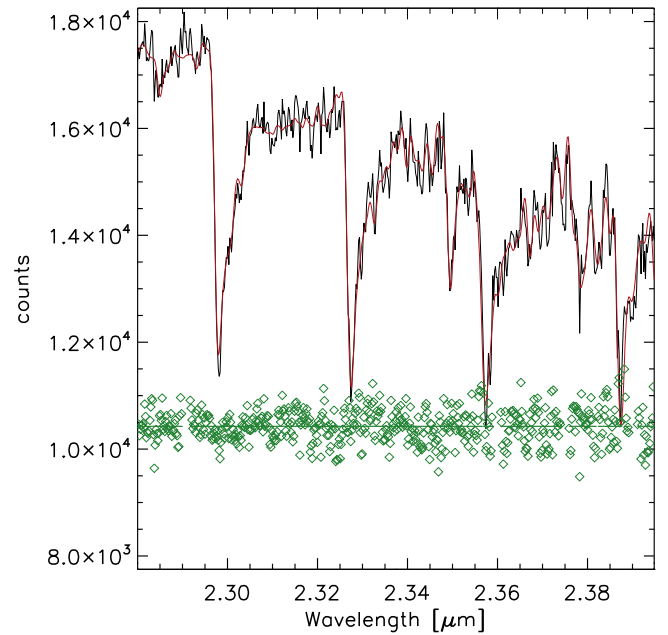


**Figure 4.** Integrated ( $r < 0''.75$ ) spectrum of M59-UCD3 shown in black. The red line indicates the best kinematic fit, and residuals are shown in green. For visibility, the residuals are offset by  $1.04 \times 10^4$  counts. The integrated dispersion was found to be  $\sigma = 65.7 \pm 0.6\ \text{km s}^{-1}$  with a median  $\text{S/N} = 57$  per pixel.

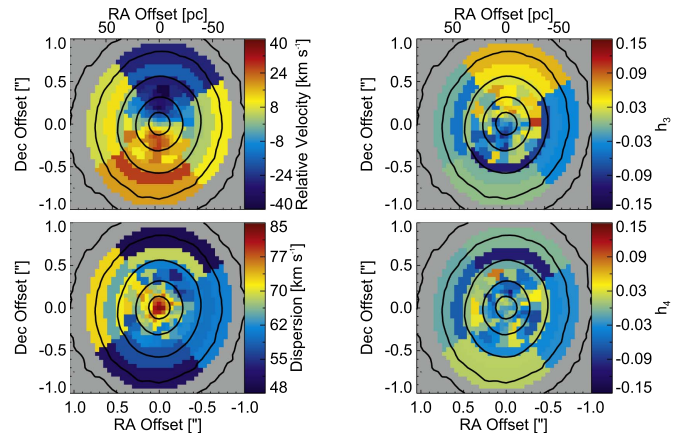


**Figure 5.** Full kinematic measurements of M59-UCD3, which include the radial velocity (top left), dispersion (bottom left), skewness  $h_3$  (top right), and kurtosis  $h_4$  (bottom right). Black contours show the  $K$ -band continuum at  $1\ \text{mag arcsecond}^{-2}$  intervals. The median  $1\sigma$  uncertainties are  $3.9\ \text{km s}^{-1}$  for the velocity,  $3.7\ \text{km s}^{-1}$  for dispersion,  $0.04$  for  $h_3$ , and  $0.05$  for  $h_4$ . Here  $h_3$  clearly shows the common anticorrelation with the velocity.

radii, with both the dispersion and rotation decreasing outward. This is similar to the  $V/\sigma$  of  $0.3\text{--}0.5$  seen in other UCDs, including M60-UCD1 and VUCD3 (Seth et al. 2014; Ahn et al. 2017; Voggel et al. 2018). This level of rotation is higher than what is seen in any Milky Way GCs (e.g., Kimmig et al. 2015; Kamann et al. 2018) and is within the range of nearby galaxy nuclei with resolved observations (e.g., Feldmeier et al. 2014; Nguyen et al. 2017).

### 3. Dynamical Modeling

In this section we present our dynamical modeling techniques and their results. Here we present three techniques: JAM, axisymmetric Schwarzschild modeling, and triaxial

<sup>22</sup> <http://davor.krajnovic.org/idl/>



**Table 3**  
Gemini/NIFS Kinematic Measurements

Bin Number	X rad (pixels)	Y rad (pixels)	Number of Pixels	S/N	$\chi^2$	$v$ (km s <sup>-1</sup> )	$v_{\text{err}}$ (km s <sup>-1</sup> )	$\sigma$ (km s <sup>-1</sup> )	$\sigma_{\text{err}}$ (km s <sup>-1</sup> )	$h_3$	$h_{3,\text{err}}$	$h_4$	$h_{4,\text{err}}$
...	...	...	...	...	...	...	...	...	...	...	...	...	...
15	-2.000	-4.866	3	35.02	0.603	473.92	2.93	65.77	3.04	-0.04	0.04	-0.04	0.03
16	-1.000	-4.440	2	36.09	0.541	475.05	3.36	71.81	3.73	-0.05	0.04	-0.03	0.04
17	0.000	-4.000	1	36.13	0.343	478.13	4.53	71.03	4.84	-0.05	0.05	-0.03	0.05
...	...	...	...	...	...	...	...	...	...	...	...	...	...

**Note.** Only a portion of this table is shown here to demonstrate its form and content. A machine-readable version and a FITS file containing the locations of each bin are available in the online Journal.

Schwarzschild modeling (but using an axisymmetric shape and mass model). Previous studies have shown that these techniques typically provide consistent results in estimating BH masses (e.g., Verolme et al. 2002; Cappellari et al. 2010; van den Bosch & de Zeeuw 2010; Seth et al. 2014; Drehmer et al. 2015; Feldmeier-Krause et al. 2017; Krajnović et al. 2018).

We note that our dynamical modeling effort and interpretation for M59-UCD3 are more complicated than for any previous results on BHs in UCDs (Seth et al. 2014; Ahn et al. 2017; Afanasiev et al. 2018; Voggel et al. 2018). This is in part due to the high quality of the data, which enabled us to run triaxial Schwarzschild models in addition to the JAM models (as we also did in M60-UCD1; Seth et al. 2014), and in part due to the lower BH mass fraction in M59-UCD3 relative to previous UCD detections. Our initial results showed that the triaxial Schwarzschild and JAM codes gave inconsistent results for our BH mass, which led us to also run additional axisymmetric Schwarzschild models. We were unable to fully resolve the differences here, but we do our best to weigh the evidence from these models, and in Section 3.4 we conclude that there is evidence for a  $\sim 2\%$  mass fraction BH in M59-UCD3. We discuss each modeling method individually below before reaching these conclusions.

### 3.1. Jeans Anisotropic Models

We use the JAM method to fit the  $V_{\text{rms}} = \sqrt{V^2 + \sigma^2}$  using the code<sup>19</sup> described in Cappellari (2008). This technique solves the anisotropic Jeans equations under two general assumptions: (1) the velocity ellipsoid is aligned with the cylindrical coordinate system ( $R, z, \phi$ ), and (2) the anisotropy is constant and defined as  $\beta_z = 1 - (\sigma_z/\sigma_R)^2$ , where  $\sigma_z$  is the velocity dispersion parallel to the rotation axis and  $\sigma_R$  is the velocity dispersion in the radial direction (Cappellari 2008). The primary input ingredients for the JAM models are the mass and luminosity density model (parameterized by MGEs as described in Section 2.1). These define the gravitational potential and the distribution of the tracer population that produces the observed kinematics. We use the JAM code to fit the following parameters: (1) the intrinsic axial ratio, which acts as a parameterization of the inclination angle ( $q = \frac{\sqrt{q'^2 - \cos^2 i}}{\sin i}$ , where  $q$  is the parameter we sample over and  $q'$  is the axis ratio of the flattest MGE); (2) the mass of a point-like BH  $M_{\text{BH}}$ ; (3)  $\Gamma$ , which parameterizes the  $M/L$  relative to the best-fit stellar population estimate; and (4) the anisotropy parameter  $\beta_z$  (see Section 3.1 of Cappellari (2008) or Section 4 of Ahn et al. (2017) for a more detailed explanation of how these parameters are used). For a given set

of these four parameters, the JAM model generates observable model kinematic measurements that can be compared with the measured values.

For our JAM dynamical models we created a Markov Chain Monte Carlo (MCMC) simulation to fully sample parameter space. The parameters sampled include the axial ratio, anisotropy parameter ( $\beta_z$ ),  $\Gamma$ , and mass of the BH. We used the *emcee* python package<sup>23</sup> developed by Foreman-Mackey et al. (2013), which is an implementation of the affine-invariant MCMC ensemble (Goodman & Weare 2010). This algorithm uses a set of walkers to explore the parameter space. At each step, the result of the likelihood for each walker informs the next choice of model parameters to be evaluated. We ran all of our models with 200 steps per walker.

#### 3.1.1. Default Model

For our default model, we used the  $K$ -band luminosity model to represent the tracer population, the mass model determined from the fixed F814W surface brightness profile fit to represent mass distribution, and the best-fit Gauss+Moffat function PSF (all described in Section 2). We ran our MCMC chain for this default model with 100 walkers for a total of 20,000 steps. We consider the first 50 steps of each walker as the burn-in phase. Figure 6 shows the post burn-in phase distributions for this model. Here the scatter plots show the two-dimensional distributions for each parameter, with points colored according to their likelihood (white: high; blue/black: low). The histograms show the one-dimensional distributions for each parameter. We used the one-dimensional distributions to calculate the best-fit values and their corresponding uncertainties. The axis ratio is nearly unconstrained. The best-fit  $\beta_z = 0.1 \pm 0.1$ . We also see a slight degeneracy between  $\beta_z$  and both  $\Gamma$  and the mass of the BH ( $M_{\text{BH}}$ ). The degeneracy seen here is less significant than we found in our previous study (Ahn et al. 2017), which we attribute to our higher-quality kinematic data. The best-fit  $\Gamma = 0.64 \pm 0.02$  (which corresponds to  $M/L_{\text{dyn},F814W} = 1.58 \pm 0.05$  or  $M/L_{\text{dyn},V} = 2.69 \pm 0.08$ ) and  $M_{\text{BH}} = (5.9 \pm 1.1) \times 10^6 M_{\odot}$ . The degeneracy between  $M_{\text{BH}}$  and  $\Gamma$  is expected, well known, evident across all of our dynamical modeling techniques (shown in Figure 10, where blue contours represent the JAM models), and similar to what has been seen in previous studies (Seth et al. 2014; Ahn et al. 2017; Voggel et al. 2018). Here we quote the  $1\sigma$  uncertainties calculated from the 16th and 84th percentiles of the one-dimensional MCMC distributions. Due to the lack of orbital freedom in the JAM models, we also quote the  $3\sigma$  uncertainties (0.2 and 99.8 percentiles), which encompass the

<sup>23</sup> <https://github.com/dfm/emcee>

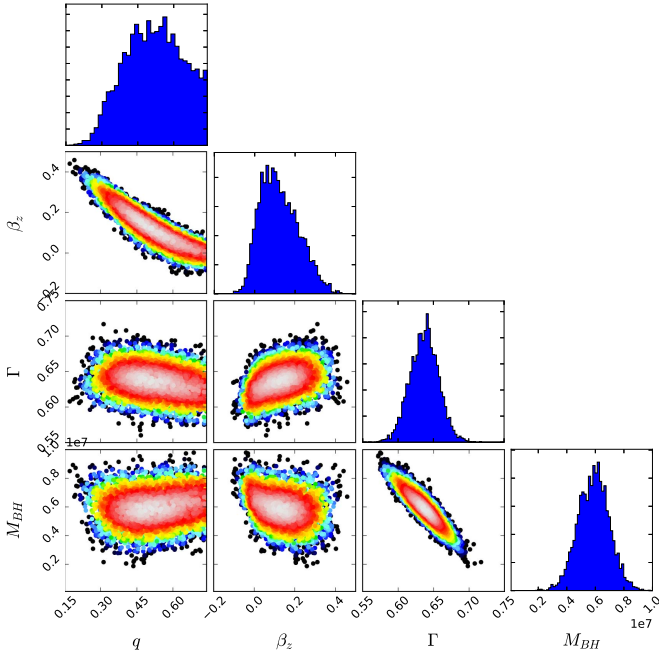


**Figure 6.** MCMC post burn-in phase distributions for our default model. The scatter plots show the projected two-dimensional distributions for each parameter. The histograms show the projected one-dimensional distribution. From top left to bottom right the panels show the axis ratio, anisotropy parameter  $\beta_z$ ,  $\Gamma$ , and  $M_{\text{BH}}$ .

systematic effects, discussed below. Quoting  $3\sigma$  errors, we find  $\beta_z = 0.1^{0.3}_{-0.2}$ ,  $\Gamma = 0.64 \pm 0.06$  ( $M/L_{\text{dyn},\text{F814W}} = 1.58 \pm 0.15$ ,  $M/L_{\text{dyn},\text{V}} = 2.69 \pm 0.25$ ), and  $M_{\text{BH}} = (5.9 \pm 3.1) \times 10^6 M_{\odot}$ . Figure 7 shows the comparison of the smoothed data with the model  $V_{\text{rms}}$  calculated with the best-fit parameters.

### 3.1.2. Quantifying the Systematic Effects

To quantify the systematic effects of our choice of the default model (discussed above), we also ran MCMC chains with 100 walkers and 20,000 total steps. To demonstrate the effects of each systematic effect, we varied the PSF, mass model, and luminosity model one by one, while holding the other parameters fixed to our default model. The cumulative likelihood for all model variations is shown in Figure 8. The black line represents the default model described above, with gray lines indicating the  $1\sigma$  and  $3\sigma$  uncertainties. The colored lines show variations in the PSF (red), mass model (blue), and luminosity model (cyan), which are explained in more detail below.

The PSF is the largest source of systematic errors, seen in Figure 8 as the red lines. Our default PSF was the best-fit model to the NIFS continuum image from the  $K$ -band model. The solid line represents a double-Gaussian model PSF, and the dashed line represents a Gauss+Moffat function model PSF where the central Gaussian FWHM is assumed to have an  $\text{FWHM} = 0''.07$ , which is the diffraction limit of the NIFS instrument. In this model PSF, the Moffat function FWHM was left unchanged from the default PSF, but the corresponding weights of the Gauss and Moffat functions were recalculated to match the NIFS continuum. In all of the dynamical modeling techniques the model predictions are convolved with the kinematic PSF before comparison with the data (see Appendix A of Cappellari 2008). Therefore, our determination of the kinematic PSF is crucial in generating model observables

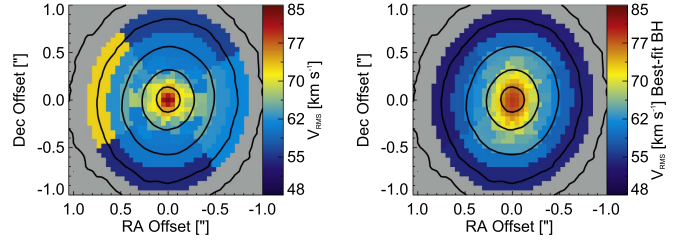


**Figure 7.**  $V_{\text{rms}}$  comparison between the smoothed data (left) and best-fit JAM model (right). Black contours show isophotes in the  $K$ -band stellar continuum. We note that we smoothed the kinematic data in this figure for visual comparison only.

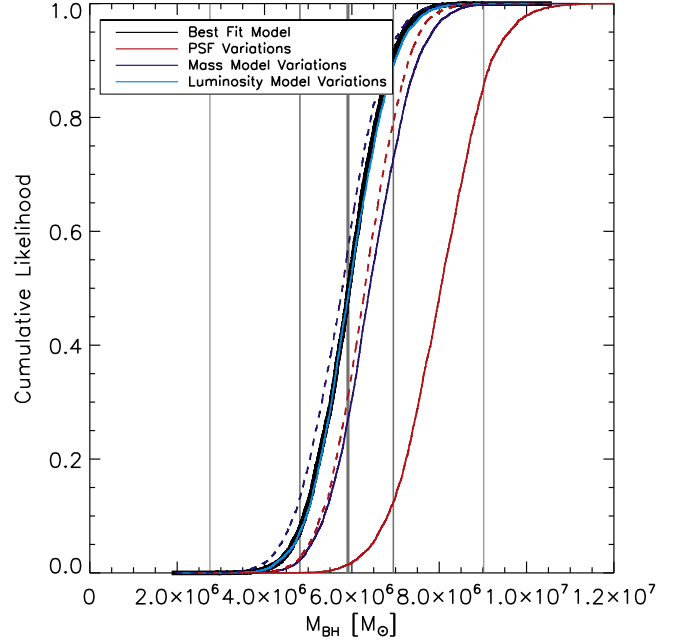


**Figure 8.** Cumulative likelihood of  $M_{\text{BH}}$  from the JAM modeling. The black line represents the best fit of the default model. The colored lines represent variations in the PSF (red), mass model (blue), and luminosity model (cyan). The gray vertical lines indicate the best fit,  $1\sigma$ , and  $3\sigma$  BH mass estimates based on the default model. See Section 3.1 for a detailed explanation the individual red, blue, and cyan lines.

that match the data. We tested the double-Gaussian PSF, as it is a common way to represent the adaptive optics PSF (but we clearly did not fit the radial profile of the NIFS continuum as well in our case). We also tested a PSF created by convolving of the F814W image as opposed to our  $K$ -band model and found very similar results (line not shown). The diffraction-limited PSF was tested owing to our inability to match the central few pixel  $V_{\text{rms}}$  values. As shown in Figure 9, the best-fit parameters with the diffraction-limited PSF allow the model  $V_{\text{rms}}$  values to better match the data near the center but have minimal effect on the BH mass. Here we took an elongated rectangular aperture along the semimajor (red) and semiminor (blue) axes. The solid lines represent the best-fit model  $V_{\text{rms}}$  with the default model, and the dashed lines represent the best-fit model with the diffraction-limited PSF. Despite the better fit to the central data, we prefer our default model, as the diffraction-limited NIFS PSF, convolved with a model of the  $HST$  photometry, provides a worse fit to the surface brightness inferred from the NIFS data cube.

The blue lines in Figure 8 represent mass model variations with the default luminosity model and PSF. In this case, the



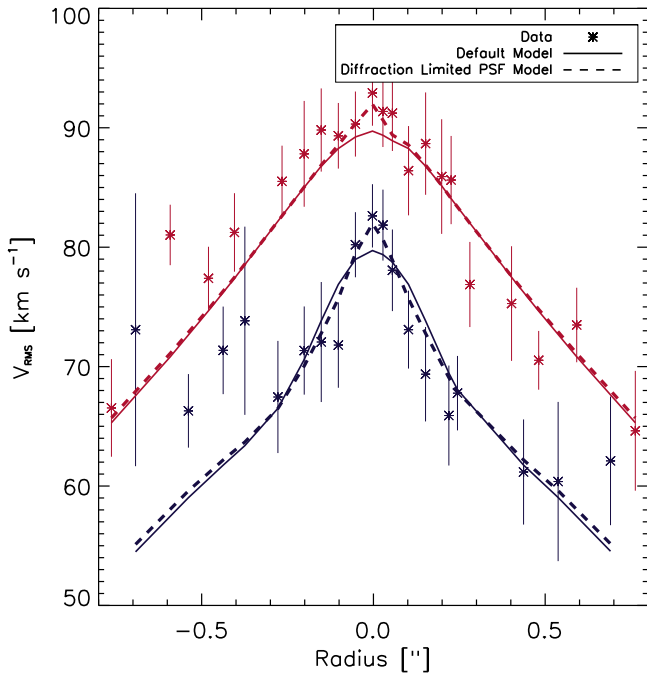


**Figure 9.**  $V_{\text{rms}}$  comparison between the data, best-fit default JAM model (solid line with  $M_{\text{BH}} = 5.9 \times 10^6 M_{\odot}$ ,  $\Gamma = 0.64$ ), and best-fit diffraction-limited PSF JAM model (dashed line with  $M_{\text{BH}} = 6.3 \times 10^6 M_{\odot}$ ,  $\Gamma = 0.63$ ). Here we take an elongated rectangular aperture one pixel wide along the semimajor axis (red) and the semiminor axis (blue). The semimajor axis has been offset by  $10 \text{ km s}^{-1}$  for visibility.

solid line shows a mass model that was determined from the color of the free Sérsic profile fits at the FWHM of each Gaussian in the MGE. This variation was motivated by the uncertainty in determining our mass profile from the fixed Sérsic models. The dashed line shows our mass-follows-light model, which is equivalent to scaling all of the Sérsic components by the flux-weighted  $M/L$  ( $M/L_{\text{F814W},*} = 2.47$ ). This test was motivated by the bluer color of the outer component, which could also be due to an older, more metal-poor population at larger radii. The de-extincted color of this component is redder than the Bruzual & Charlot (2003) models for metallicities below  $Z = 0.004$  ( $[\text{Fe}/\text{H}] \sim -0.7$ ). If we assume a model at that metallicity, we get an  $M/L_{\text{F814W},*} = 1.9$ ; this is closer to (but still lower than) the inner-component  $M/L$ s, and thus the resulting mass profile is intermediate between our constant  $M/L$  and default model  $M/L$ s. Figure 8 shows that these mass model variations provide  $M_{\text{BH}}$  constraints within the  $1\sigma$  deviations from the default model, and therefore our results do not depend critically on the stellar population variations.

Finally, the cyan line represents a luminosity model variation where we used the default mass model and PSF but the original fixed F814W luminosity MGE. The luminosity model variation makes the least difference. This is expected since the luminosity model is only used to determine the center of each kinematic bin and generate the observed kinematic field. Figure 8 shows that our choice for the default model is reasonable given that all of the model variations fall within the  $3\sigma$  error bars calculated from the default model likelihood.

### 3.2. Axisymmetric Schwarzschild Models

We fit the full line-of-sight velocity distribution (LOSVD) using an axisymmetric Schwarzschild orbit superposition

model described in detail in Cappellari et al. (2006). This three-integral dynamical modeling technique is based on Schwarzschild’s numerical orbit superposition method (Schwarzschild 1979), which has been shown to reproduce kinematic observations (Richstone & Tremaine 1988; Rix et al. 1997; van der Marel et al. 1998). This method assumes axisymmetry, which also requires the potential to not vary on the timescale required to sample the density distribution of an orbit. Since the orbital timescale within M59-UCD3 is  $\sim 10^6$  yr (assuming our effective radius and integrated dispersion), while the relaxation time is  $\sim 10^{12}$  yr and the orbital timescale of M59-UCD3 around M59 is  $\sim 10^8$  yr, the potential is unlikely to vary during the orbital sampling period. The generality of this method has allowed it to become the standard for determining the mass of central BHs when high-resolution kinematic data are available (e.g., Cappellari et al. 2002; Verolme et al. 2002; Gebhardt et al. 2003; Valluri et al. 2005; Shapiro et al. 2006; van den Bosch et al. 2006; Nowak et al. 2007, 2008; Cappellari et al. 2009; Krajnović et al. 2009). However, the more general approach, which allows for triaxial systems, is described in van den Bosch et al. (2008) and discussed in Section 3.3.

The full details of this method are described in Cappellari et al. (2006). In short, this method consists of four steps. First, as with the JAM models, a stellar potential is created by deprojecting the mass model MGEs assuming an axisymmetric shape and stellar  $M/L$ . Second, a representative, dithered orbit library is constructed with even sampling across the observable sampling space (based on the three integrals of motion and the stellar potential). Next, the orbits are projected onto the observable space using sky positions and taking into account the kinematic PSF and apertures (Voronoi bins, discussed in Section 2.2). Finally, the weights of each orbit are determined using a non-negative least-squares fit (Lawson & Hanson 1974) and are co-added to reproduce the observed kinematics.

For our models, we follow the approach outlined in Krajnović et al. (2009), with the only exception being that for M59-UCD3 we do not assume that mass follows light. We used our default model, described above, to construct the mass and luminosity profiles. Here the mass MGE is used to calculate the orbit libraries. For these models, we fixed the inclination angle to be  $85^\circ$ . This choice was arbitrary, as the inclination angle has virtually no effect on the mass of the BH and  $\Gamma$  (see Section 3.1). We created a grid of the two free parameters:  $M_{\text{BH}}$  and  $\Gamma$ . The orbit libraries are constructed for each  $M_{\text{BH}}$  at an expected  $\Gamma$  and consist of  $21 \times 8 \times 7 \times 2$  orbital bundles, which are composed of  $6^3$  dithers (see Cappellari et al. 2006). This means that there are 508,032 total orbits, of which 2352 are free to vary to optimize the fit. It is not necessary to compute an orbit library for every ( $M_{\text{BH}}$ ,  $\Gamma$ ) combination because the orbit libraries can be scaled to match different  $\Gamma$  values. For our grid, we sampled 32  $M_{\text{BH}}$  values between  $2 \times 10^4 M_{\odot}$  and  $1.2 \times 10^7 M_{\odot}$  and 47  $\Gamma$  values between 0.43 and 0.89. The red contours in Figure 10 show the  $1\sigma$ ,  $2\sigma$ , and  $3\sigma$  contour results for  $\Gamma$  and  $M_{\text{BH}}$ . These contours were calculated from the LOESS smoothed  $\chi^2$  distribution. Likewise, the best fits determined from the likelihood distribution are  $M_{\text{BH}} = 2.5^{+1.8}_{-1.3} \times 10^6 M_{\odot}$  and  $\Gamma = 0.67 \pm 0.03$  ( $1\sigma$  uncertainties from the 16th and 84th percentiles). We note that these models are consistent with no BH within the  $3\sigma$  contour.

Figure 10 also shows a similar size and overlap between the  $1\sigma$  uncertainties from the axisymmetric Schwarzschild models

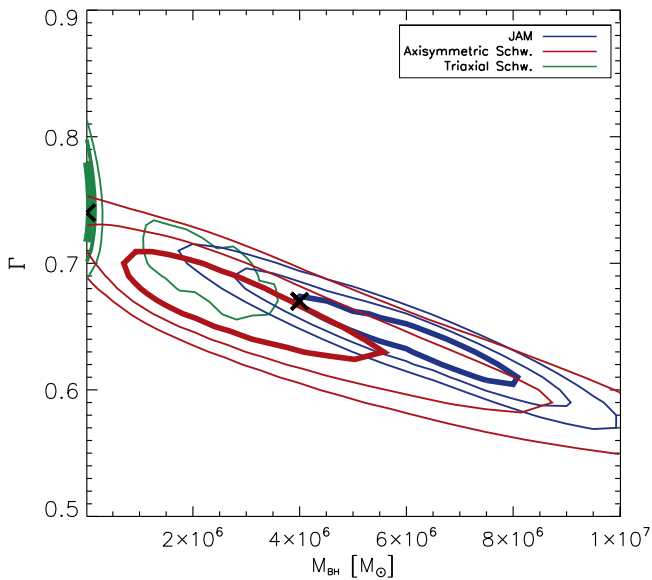


**Figure 10.** Contour plots showing all three modeling techniques. Here the blue contours represent the JAM models red contours are the axisymmetric Schwarzschild models, and green contours are the triaxial Schwarzschild models. The black crosses denote the BH mass and  $\Gamma$  values used to make the  $V_{\text{rms}}$  comparison plot shown in Figure 11.

(red contours) and the JAM models (blue contours). However, we note that these are formal errors and are smaller for JAM owing to the reduced freedom of the model.

### 3.3. Triaxial Schwarzschild Models

Finally, we also fit the full LOSVD using the more general triaxial Schwarzschild models and corresponding code described in detail in van den Bosch et al. (2008). This model is also based on Schwarzschild’s numerical orbit superposition method (Schwarzschild 1979) but is not restricted to axisymmetry as described above. This method is implemented in a series of steps, similar to those described in Section 3.2. First, the stellar potential is created by deprojecting the mass model MGE, as described above. However, in the triaxial case, the viewing angles must be provided, which parameterize the intrinsic shape of the galaxy (see Section 3 of van den Bosch et al. 2008). Second, the initial conditions for each orbit library are found. These orbits must include all possible types of orbits that the potential can support (Thomas et al. 2004; van den Bosch et al. 2008). Next, the orbits are integrated for a fixed period of time, while storing the projected properties on a grid for comparison with the data. These properties are convolved with the same PSF as the kinematic observations. Finally, the orbital weights are determined using a sparse quadratic programming solver from the GALAHAD library, which is capable of fitting the kinematics in a least-squares sense while also satisfying the mass constraints (Gould et al. 2003).

For M59-UCD3, we provided an oblate axisymmetric shape by specifying the viewing angles  $(\theta, \phi, \psi) = (85^\circ, -49^\circ 99', 89^\circ 99')$ . In the oblate limit, the model does not depend on  $\phi$ , while  $\psi$  must be  $90^\circ$ , and  $\theta$  represents the inclination angle. Therefore, our model is nearly axisymmetric and seen at an inclination angle of  $85^\circ$ . The choice of the inclination angle was again arbitrary, but it matches the axisymmetric Schwarzschild models. We sampled over all possible inclination angles and found consistent results. With this setup, the triaxial Schwarzschild models are sampled in

the axisymmetric limit but still allow for all possible orbits in a triaxial potential. For the other two parameters,  $\Gamma$  and  $M_{\text{BH}}$ , we created a grid similar to the axisymmetric Schwarzschild models described above. We sampled 47  $M_{\text{BH}}$  values ranging from  $5.5 \times 10^3$  to  $2 \times 10^7 M_\odot$  and 62  $\Gamma$  values ranging from 0.43 to 1.04. The main results are shown as green contours in Figure 10. Here the best-fit  $\Gamma = 0.75 \pm 0.06$ , and we find that  $M_{\text{BH}}$  is consistent with no BH.

There is a clear disagreement on  $M_{\text{BH}}$  between the JAM models/axisymmetric Schwarzschild models and these triaxial Schwarzschild models. To attempt to resolve these differences, we explored a wide range of tests for our triaxial models, including fitting only the inner higher-S/N region, fitting sectors of the data, symmetrizing the kinematics, fitting only the radial velocity and velocity dispersion, adding various amounts of regularization, changing the total number of integrated orbits, and varying the input models and PSFs. In every test, the fitting results remained consistent. However, we note two interesting observations:

- (1) The green contours shown in Figure 10 show significant  $\chi^2$  differences in the model in the region  $M_{\text{BH}} < 2 \times 10^5 M_\odot$ . At these masses, the BH sphere of influence is  $< 0'' 002$ , which is well below the diffraction limit of our NIFS data. This is clearly unphysical, as the data cannot possibly constrain BH masses in this low-mass regime (i.e., the green contours are closed well below the diffraction limit of our instrument). We note that if we ignore models with  $M_{\text{BH}} \lesssim 3 \times 10^5$  the triaxial model results become fully consistent with the JAM models/axisymmetric Schwarzschild models.
- (2) We calculated the  $\chi^2$  value for each of the model kinematic moments and  $V_{\text{rms}}$  independently. These values for two model BH masses are shown in Table 4, which shows that the even kinematic moments and the  $V_{\text{rms}}$  favor a high-mass BH. However, the overall fit is clearly being driven by the odd velocity moments, especially the radial velocity. This is also unphysical, as the odd moments are supposed to provide virtually no constraints on the gravitational potential, as they have large freedom to vary, at fixed potential, to fit the data. As discussed in Section 3.4, comparing the  $V_{\text{rms}}$  profiles of the best-fit no BH with a best-fit  $M_{\text{BH}} \sim 4 \times 10^6 M_\odot$  shows a significantly better fit to the central pixels in the latter case. These observations lead us to speculate that the minimum  $\chi^2$  at zero BH may be a numerical artifact and to favor the results from the JAM and axisymmetric Schwarzschild models of a detectable SMBH.

### 3.4. Summary of Dynamical Results

In summary, we detect a central massive BH with the JAM dynamical models where the best-fit  $M_{\text{BH}}$  and  $\Gamma$  are  $(5.9 \pm 1.1) \times 10^6 M_\odot$  and  $0.64 \pm 0.02$ , respectively. With the axisymmetric Schwarzschild models we find the best-fit  $M_{\text{BH}} = 2.5^{+1.8}_{-1.3} \times 10^6 M_\odot$  and  $\Gamma = 0.67 \pm 0.03$  ( $1\sigma$  uncertainties). Finally, with the triaxial Schwarzschild models we find that the results are consistent with no BH and  $\Gamma = 0.75$ . However, the triaxial models show a small region that overlaps with the JAM/axisymmetric Schwarzschild models at the  $3\sigma$  level.

Despite the variations in the dynamical modeling results, all of the models provide better fits to the  $V_{\text{rms}}$  data with a BH

**Table 4**  
Calculations of Triaxial Schwarzschild Model Reduced  $\chi^2$  Independently

$M_{\text{BH}} (M_{\odot})$	$\Gamma$	$\chi^2$ Total LOSVD	$\chi^2$ Vel Only	$\chi^2 \sigma$ Only	$\chi^2 h_3$ Only	$\chi^2 h_4$ Only	$\chi^2 V_{\text{rms}}$
$10^4$	0.75	0.765	1.005	0.875	0.791	0.498	0.799
$4 \times 10^6$	0.65	0.793	1.072	0.819	0.805	0.494	0.753

mass in the range of  $(2-6) \times 10^6 M_{\odot}$ . This is particularly true in the central pixels, as shown in Figure 11. Here we show a  $V_{\text{rms}}$  model comparison for all of the dynamical modeling techniques along the semimajor axis. The colored lines show the JAM (blue), axisymmetric Schwarzschild model (red), and triaxial Schwarzschild model (green) best-fit parameters for two hypothetical  $M_{\text{BH}}$ ,  $\Gamma$  combinations, shown as crosses in Figure 10. In this case, we show an  $M_{\text{BH}} \sim 4 \times 10^6 M_{\odot}$  with  $\Gamma = 0.67$  as solid lines and  $M_{\text{BH}} \sim 10^4 M_{\odot}$  with  $\Gamma = 0.74$  as dashed lines. It is clear from this comparison plot that the high-mass BH is favored in the  $V_{\text{rms}}$  profile for all of the dynamical modeling techniques, especially near the center, where we expect that the effects of a central massive BH are the most significant.

The results of the dynamical modeling techniques show that we cannot constrain the lower limit of the mass of a central massive BH. However, the better fits to the central  $V_{\text{rms}}$  profiles provide evidence in favor of a detectable BH mass. Furthermore, the JAM and axisymmetric Schwarzschild models are nearly consistent at the  $1\sigma$  level. By combining the  $1\sigma$  confidence levels of the JAM and axisymmetric Schwarzschild models, we suggest that the BH mass in M59-UCD3 is  $M_{\text{BH}} = 4.2^{+2.1}_{-1.7} \times 10^6 M_{\odot}$ . This estimate is based on the average of the best-fit JAM and axisymmetric Schwarzschild models, where the uncertainties from each model were added in quadrature. We do the same for the best  $\Gamma$  value to find  $\Gamma = 0.65 \pm 0.04$ , which corresponds to an average  $M/L_{\text{F814W,dyn}} = 1.61 \pm 0.10$  and  $M/L_{V,\text{dyn}} = 2.73 \pm 0.17$ .

Finally, we note that this study is, to our knowledge, the first time that a direct comparison has been made between these three dynamical modeling codes. As noted at the beginning of this section, in general, comparisons of JAM and Schwarzschild modeling have found consistent results. One interesting recent study by Leung et al. (2018) has compared both Schwarzschild and JAM models against circular velocities derived from molecular gas for 54 galaxies with CALIFA integral field stellar kinematics. The study found that JAM and Schwarzschild recover consistent mass profiles, without evidence for systematic biases (their Figure D1). However, it also found that the JAM recovers more reliable circular velocities than the Schwarzschild models in the large-radii regime, where the gas velocities are more reliable (their Figure 8). Although the study was not specific to SMBHs, it shows that the reduced generality of the JAM method, with respect to Schwarzschild's, can lead to a more robust mass-profile recovery from real observations. The lack of flexibility could be leading to a more robust result here too, especially if the kinematic data include any outliers that are not well described by their error bars. Finally, we note that despite the disagreement in the BH mass, the overall agreement between the models is quite good; apart from the triaxial Schwarzschild model  $\chi^2$  minimum at zero BH mass, the confidence regions of all three models overlap in both  $\Gamma$  and  $M_{\text{BH}}$ .

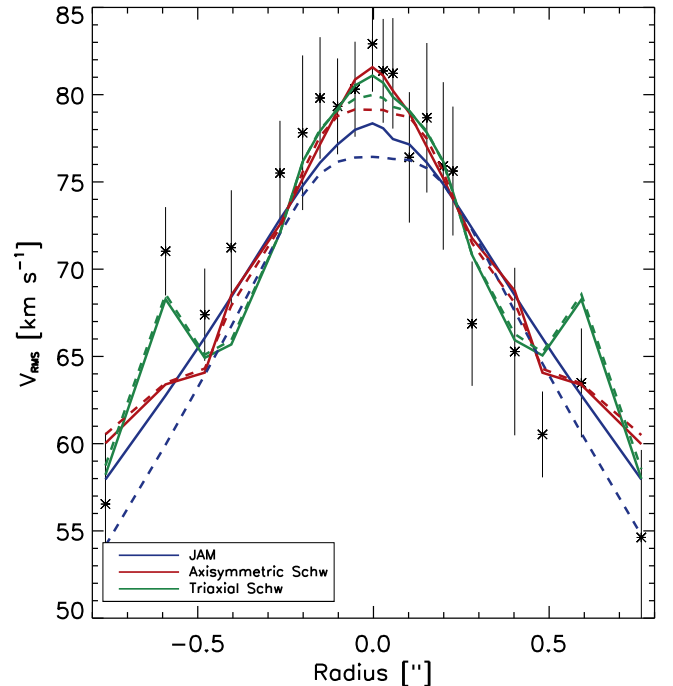


**Figure 11.** Black points show a rectangular aperture along the semimajor axis. The solid lines represent a model  $\sim 4 \times 10^6 M_{\odot}$  BH with  $\Gamma = 0.67$  for the JAM (blue), axisymmetric Schwarzschild model (red), and triaxial Schwarzschild model (green). The dashed line represents a  $\sim 10^4 M_{\odot}$  BH with  $\Gamma = 0.74$  using the same colored convention described above. Note that these  $M_{\text{BH}}$ ,  $\Gamma$  combinations are not the best-fit model from any of the dynamical models. This choice is arbitrary and is for visual comparison between a low- and high-mass BH only.

#### 4. Radio and X-Ray Observations of UCDs

An alternative method for inferring the presence of an SMBH in UCDs is via accretion, which produces X-ray and radio emission. X-ray emission alone is only suggestive, as low-mass X-ray binaries (LMXBs) are common in dense stellar systems and can mimic the X-ray emission from a low-luminosity active galactic nucleus (AGN). However, radio emission from LMXBs is not detectable at the distance of the Virgo Cluster and hence is a more secure indication of an SMBH.

Here we consider the radio and X-ray emission from three massive UCDs around the Virgo galaxies M59 and M60: M59c0, M59-UCD3, and M60-UCD1, which all have dynamical evidence for SMBHs. We note that no deep radio data exist for the other UCDs with evidence of SMBHs.

##### 4.1. Radio

We obtained deep radio continuum data for M59 and M60 with the Karl G. Jansky Very Large Array (VLA) as part of program 15A-091 (PI: Strader) in 2015 February and March. All data were taken in B configuration and with C band receivers in 3-bit mode, split into subbands centered at 5 and



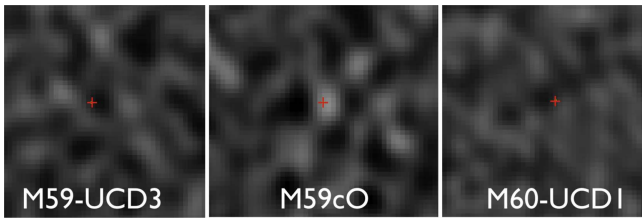


**Figure 12.** VLA images of a  $10''$  (800 pc) box around three massive UCDs with dynamical evidence for SMBHs: M59-UCD3, M59cO, and M60-UCD1. The red plus signs mark the optical positions of the UCDs. M59cO has evidence for an associated radio source as discussed in the text, while M59-UCD3 and M60-UCD1 are not detected in the VLA images.

7 GHz, each with 2 GHz of bandwidth. Four 1.75 hr long blocks were observed, and in each block observations alternated between the two targets, giving 3.5 hr of observations (2.6 hr on source) per galaxy. The data were flagged and calibrated in AIPS using standard methods and then imaged with Briggs robust weighting (Briggs 1995). The subband data were imaged separately (at central frequencies of 4.6 and 7.1 GHz after flagging) and together, at a mean frequency of 5.8 GHz. The beam in the combined images is  $1''.33 \times 1''.14$ .

M59-UCD3 is not detected in the individual subbands or in the combined image. The local rms noise in the region of M59-UCD3 is  $2.6 \mu\text{Jy beam}^{-1}$ . Hence, we set a  $3\sigma$  upper limit of  $<7.8 \mu\text{Jy beam}^{-1}$  ( $L < 1.27 \times 10^{34}$ ) at a mean frequency of 5.8 GHz. M60-UCD1 is also undetected, with a local rms of  $2.4 \mu\text{Jy beam}^{-1}$  and a corresponding upper limit of  $<7.2 \mu\text{Jy beam}^{-1}$  ( $L < 1.17 \times 10^{34}$ ) at 5.8 GHz. In contrast, we do detect M59cO in the 4.6 GHz subband at a flux density of  $10.8 \pm 3.8 \mu\text{Jy beam}^{-1}$  ( $L = 1.75 \times 10^{34}$ ). It is not detected in the 7.1 GHz image. The UCD is detected in *Gaia* with a J2000 position of (R.A., decl.) = (12:41:55.334, +11:40:03.79), only  $0''.1$  from the VLA position of the radio source in the 4.6 GHz image (R.A., decl.) = (12:41:55.331, +11:40:03.69). The astrometric match suggests that the radio emission, while faint, is indeed real and associated with M59cO. Here the luminosity is the flux density in  $\mu\text{Jy} \times 10^{-29} \times 4\pi R^2 \times 5 \times 10^9$ . These are all given at 5 GHz (i.e., assuming a flux density slope of  $\alpha = 0$  (flat)). VLA mosaic images for these three UCDs are shown in Figure 12.

#### 4.2. X-Ray

These UCDs have been studied in the X-rays using *Chandra* by several previous authors (Luo et al. 2013; Strader et al. 2013; Hou & Li 2016; Pandya et al. 2016), but we revisit this analysis to ensure consistency. All our results are consistent with these past studies. As noted in these previous studies, the X-ray emission from UCDs can be explained by LMXBs. In fact, the number of X-ray sources falls short of expectations based on GC X-ray sources, but SMBH emission cannot be excluded (Hou & Li 2016; Pandya et al. 2016). Given that  $10^6$ – $10^7 M_\odot$  SMBHs do seem to be present in UCDs, if these are accreting at the typical Eddington ratios seen for early-type galaxies ( $L_{\text{bol}}/L_{\text{edd}} \sim 10^{-6}$  Ho 2009), we would expect the UCDs to have detectable X-ray sources of  $\sim 10^{38} \text{ erg s}^{-1}$ . As discussed further in the next section, the radio emission from LMXBs is much lower than that expected for emission from SMBHs, and thus a detection of both X-ray and radio emission from a source would provide strong evidence for SMBH accretion.

There are two separate observations of M59 (encompassing both M59-UCD3 and M59cO) and six observations of M60 that cover M60-UCD1; these are summarized in Table 4. We downloaded these observations from the *Chandra* data archive and reprocessed them using CIAO 4.9 and CalDB 4.7.6. We used a  $1''.5$  extraction radius around each source and measured the background in a larger nearby source-free area before normalizing the counts to the source extraction region size. We initially determined all counts in the 0.3–10 keV range for maximum sensitivity, but we report results in the 0.5–10 keV range for appropriate comparison to the fundamental plane. For both galaxies we fix  $N_{\text{H}} = 2 \times 10^{20} \text{ cm}^{-2}$  (taking extinction from Schlafly & Finkbeiner (2011) and conversion from Bahramian et al. (2015)). All spectral extractions were performed with CIAO task *specextract*, and spectral analysis was done using Xspec 12.9.1n (Arnaud 1996). We assumed Wilms et al. (2000) abundances and Verner et al. (1996) absorption cross sections.

M59cO is not detected in the 2001 or 2008 observations. Assuming a power law with  $\Gamma = 1.5$ , in the 2001 data we find a 95% upper 0.5–10 keV unabsorbed flux limit of  $<5.3 \times 10^{-16} \text{ erg s}^{-1} \text{ cm}^{-2}$ , equivalent to  $L_X < 1.7 \times 10^{37} \text{ erg s}^{-1}$ . The shorter 2008 data are less constraining and give a limit of  $L_X < 1.4 \times 10^{38} \text{ erg s}^{-1}$  using the same assumptions.

M59-UCD3 is detected at  $>2\sigma$  in the 2001 *Chandra* data, with a 0.5–10 keV unabsorbed flux of  $3.1^{+2.7}_{-1.7} \times 10^{-15} \text{ erg s}^{-1} \text{ cm}^{-2}$ , equivalent to  $1.0^{+0.9}_{-0.6} \times 10^{38} \text{ erg s}^{-1}$  (uncertainties are at the 95% level). Unsurprisingly, it is not detected in the factor of  $\sim 5$  shorter 2008 data. In addition, it is located near a chip gap in the 2008 observations, which makes it difficult to determine a valid upper flux limit. Here we have assumed Gehrels statistics for all of the upper limits (Gehrels 1986).

M60-UCD1 is detected in all six observations. The total merged data set, representing 308 ks of *Chandra* data, is deep enough to allow spectral fitting. After binning to 20 counts per bin, we fit the spectrum to a power law in XSPEC using *cstat*, a modified version of the Cash statistic (Cash 1979).<sup>24</sup> The best-fitting power-law index is  $\Gamma = 1.8^{+0.2}_{-0.3}$ , consistent with the  $\Gamma = 1.5$  value assumed. Hence, for consistency, we assume  $\Gamma = 1.5$  for all the flux measurements for M60-UCD1.

The individual unabsorbed 0.5–10 keV fluxes for M60-UCD1 range over  $(1.8\text{--}7.5) \times 10^{-15} \text{ erg s}^{-1} \text{ cm}^{-2}$  ( $L_X = (0.6\text{--}2.4) \times 10^{38} \text{ erg s}^{-1}$ ), depending on the epoch. The average flux is  $3.3^{+0.8}_{-0.7} \times 10^{-15} \text{ erg s}^{-1} \text{ cm}^{-2}$  ( $L_X = 1.1^{+0.3}_{-0.2} \times 10^{38} \text{ erg s}^{-1}$ ). The individual and merged fluxes are listed in Table 5.

There is compelling evidence for X-ray variability of M60-UCD1, but only at a single epoch: five of the six epochs are consistent with the mean flux, while one (ObsID 12976) is  $\sim 6\sigma$  higher compared to the mean flux. Due to the shorter exposure times and smaller number of epochs for M59-UCD3 and M59cO, we have no useful constraints on X-ray variability for these other sources.

#### 4.3. Fundamental Plane of BH Accretion

We can combine X-ray and radio detections and nondetections described above with the dynamical BH mass estimates to see whether these observations are consistent with the

<sup>24</sup> <https://heasarc.gsfc.nasa.gov/xanadu/xspec/manual/XSappendixStatistics.html>

**Table 5**  
Chandra X-Ray Constraints and Measurements

UCD ID	Obs. ID	Epoch Date	Epoch Date (MJD)	Effective Time (ks)	Flux ( $\times 10^{-15}$ erg s $^{-1}$ cm $^{-2}$ )	Luminosity ( $\times 10^{37}$ erg s $^{-1}$ )
M59-UCD3	2068	...	...	24.8	$3.1^{+2.7}_{-1.7}$	$10.1^{+8.8}_{-5.5}$
M59-UCD3	8074	...	...	5.3	...	...
M59cO	2068	...	...	24.8	<0.5	<1.7
M59cO	8074	...	...	5.3	<4.4	<14.3
M60-UCD1	785	2000-04-20	51654.148669	38.1	$1.8^{+1.3}_{-0.9}$	$5.9^{+4.2}_{-2.9}$
M60-UCD1	8182	2007-01-30	54130.521317	52.4	$3.7^{+1.7}_{-1.3}$	$12.1^{+5.5}_{-4.2}$
M60-UCD1	8507	2007-02-01	54132.122880	17.5	$3.6^{+3.7}_{-2.2}$	$11.7^{+12.1}_{-7.2}$
M60-UCD1	12976	2011-02-24	55616.730009	101.0	$7.5^{+1.6}_{-1.4}$	$24.4^{+5.2}_{-4.6}$
M60-UCD1	12975	2011-08-08	55781.313337	84.9	$2.8^{+1.2}_{-1.0}$	$9.1^{+3.9}_{-3.3}$
M60-UCD1	14328	2011-08-12	55785.067169	14.0	$2.4^{+3.3}_{-1.9}$	$7.8^{+10.8}_{-6.2}$
M60-UCD1	all	...	...	307.9	$3.3^{+0.8}_{-0.7}$	$10.8^{+2.6}_{-2.3}$

**Note.** All limits and uncertainties are at the 95% level and over the energy range 0.5–10 keV. Luminosities assume a distance of 16.5 Mpc.

fundamental plane of BH accretion (Merloni et al. 2003; Falcke et al. 2004). We note that significant variability is seen in M60-UCD1, long-term variability of low-luminosity AGNs seems to be common (e.g., Maoz et al. 2005; Hernández-García et al. 2014), and in general UCD X-ray sources appear to be variable (Hou & Li 2016; Pandya et al. 2016). Because our radio and X-ray observations are not contemporaneous, this variability adds to any intrinsic scatter present.

We use the fundamental plane of Plotkin et al. (2012),

$$\log(L_X) = (1.45 \pm 0.04)\log(L_R) - (0.88 \pm 0.06)\log(M_{\text{BH}}) - 6.07 \pm 1.10, \quad (1)$$

and plot the combinations of detections and upper limits for the three UCDs in Figure 13. We find that the radio upper limits in M59-UCD3 and especially M60-UCD1 fall well below the radio luminosities expected for objects lying on the fundamental plane. Similarly, the X-ray nondetection of M59cO is below the expectation based on its radio luminosity. However, these nondetections do not provide strong constraints on whether an accreting BH is present. This is because of the order-of-magnitude scatter in the radio luminosities relative to the fundamental plane observed in similar low-Eddington systems with known BH masses (Gültekin et al. 2009), as well as the lack of simultaneous radio and X-ray observations. Future, simultaneous detections of X-ray and radio emission in UCD BHs could provide important confirming evidence for SMBHs in these systems.

Finally, we note that from our NIFS observations we can also constrain the presence of hot dust emission in these systems. This hot dust is typically thought to be an AGN accretion signature and is found to be quite luminous in both quiescent and actively accreting BHs (Seth et al. 2010; Seth 2010; Burtscher et al. 2015). A clear correlation is seen between this emission and the X-ray and mid-infrared emission, although this correlation seems to depend significantly on AGN type (Burtscher et al. 2015). Whether this correlation continues to lower-luminosity AGNs like those observed here is not yet clear.

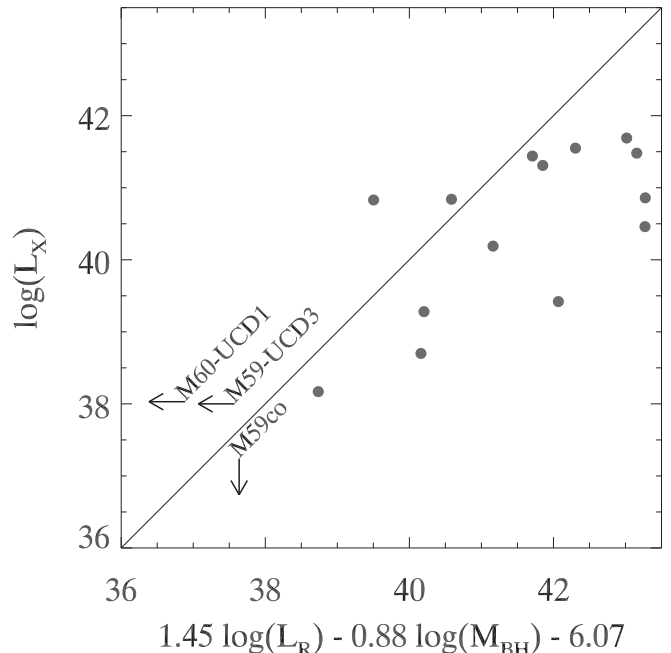


**Figure 13.** Fundamental plane for UCDs with known BHs from Plotkin et al. (2012). The radio upper limits in M60-UCD1 and M59-UCD3 and the X-ray upper limits in M59cO (arrows) are all below the predictions from the fundamental plane, but these differences are small relative to the scatter seen for similar quiescent BHs with dynamical BH mass determinations shown in gray from Gültekin et al. (2009).

## 5. Discussion and Conclusions

In this paper we have presented the results of three separate dynamical models on the most massive UCD, M59-UCD3, and discussed the radio and X-ray observations of UCDs as a way to infer the presence of SMBHs. Detections of SMBHs in UCDs provide evidence that they are the tidally stripped remnants of once more massive galaxies (Seth et al. 2014; Ahn et al. 2017; Afanasiev et al. 2018). Furthermore, the effects of the central massive BH can explain the elevated dynamical-to-stellar mass ratios detected in the most massive UCDs (Mieske et al. 2013). Nondetection of BHs can suggest either that the object is not a stripped nucleus (and instead is a massive star

cluster) or that the nucleus stripped lacked detectably massive central BHs (Voggel et al. 2018).

### 5.1. Summary of Main Results

For our analysis, we combined adaptive-optics-assisted Gemini/NIFS kinematic data with high-resolution *HST* imaging. The Gemini/NIFS data were used to determine the full LOSVD, which includes the radial velocity, velocity dispersion, skewness, and kurtosis. We found the integrated ( $r < 0''.75$ ) barycentric radial velocity to be  $V = 434.5 \pm 0.6 \text{ km s}^{-1}$  and velocity dispersion  $\sigma = 65.7 \pm 0.6 \text{ km s}^{-1}$ . The *HST* images were used to construct a mass density and luminosity profile by fitting a PSF-convolved triple-component Sérsic profile to the data. These models were used to calculate the total luminosity (within the central  $3''$ ), which we found to be  $L_{F814W} = 1.19 \times 10^8 L_{\odot}$  and an effective radius of  $0''.34$  (27 pc). The model fits suggest that the outer component of the UCD is somewhat bluer than the central components, and we modeled this stellar population variation using SSP models.

We combined these mass and luminosity density profiles with the kinematic measurements to test for the presence of a central massive BH using three dynamical modeling techniques. We summarize the results of this modeling in Section 3.4; our final conclusion is that M59-UCD3 appears to host a BH with a mass of  $M_{\text{BH}} = 4.2^{+2.1}_{-1.7} \times 10^6 M_{\odot}$ . We derive a best-fit  $\Gamma$  from the JAM and axisymmetric Schwarzschild models of  $0.65 \pm 0.04$ , which corresponds to an  $M/L_{F814W, \text{dyn}} = 1.61 \pm 0.10$  and  $M/L_{V, \text{dyn}} = 2.73 \pm 0.17$ . Therefore, the total dynamical mass is  $M_{\text{dyn}} = 1.9 \pm 0.1 \times 10^8 M_{\odot}$ .

### 5.2. Implications of a Central Massive BH

We can compare our best-fit models with a BH to those without to look at how large a change is caused in the stellar  $M/L$ . From our JAM models the best-fit zero-mass BH has a  $\Gamma$  of 0.74 ( $M/L_{V, \text{dyn}} = 3.11$ ). This represents our equivalent to the inferred mass from integrated dispersions used to determine the ratio of dynamical to population values (e.g., Mieske et al. 2013). Therefore, inclusion of a BH in the model reduces the  $M/L$  by  $\sim 12\%$ . By contrast, the  $M/L$ s drop by  $>40\%$  in all of the other UCDs with central massive BH detections (Seth et al. 2014; Ahn et al. 2017). We show the effect on  $\Gamma$  of including the BH in M59-UCD3 in Figure 14, which, by our determination, does *not* have an elevated global dynamical  $M/L$  even if there is no BH present. We note that Liu et al. (2015) estimated  $M/L_{V, \text{dyn}}$  to be  $4.9 \pm 0.5$  based on an integrated dispersion of  $77.8 \pm 1.6 \text{ km s}^{-1}$  and  $r_{\text{eff}} = 25 \text{ pc}$ , shown as an open star in Figure 14; this estimate is significantly higher than our estimates with or without a BH. Voggel et al. (2018) showed that measurements of the dynamical-to-stellar mass ratio are easily overestimated using lower spatial resolution data, which demonstrates the importance of high spatial resolution integral field unit data for determining the dynamical  $M/L$ . This is likely the reason for the discrepancy between  $M/L$ s in Liu et al. (2015) and our derived value.

In M60-UCD1, VUCD3, and M59cO, the central BH constituted 10%–20% of the total mass of the system (Seth et al. 2014; Ahn et al. 2017). M59-UCD3 is quite different, with a central BH of only  $\sim 2\%$  of the total mass. A small,  $\sim 4\%$  mass BH has also been found in Fornax UCD3 (Afanasiev

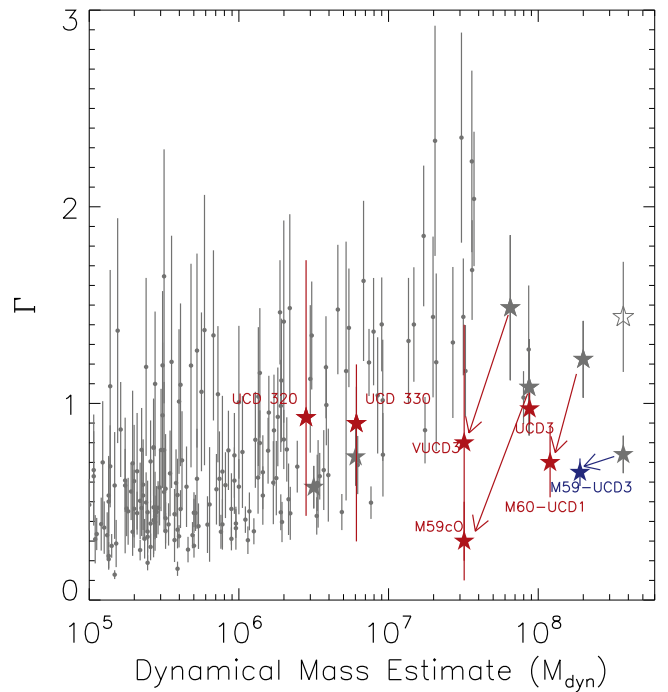


**Figure 14.** Dynamical-to-stellar mass ratio  $\Gamma$  vs. total dynamical mass. Gray points represent GCs and UCDs, where mass estimates are based on integrated velocity dispersions assuming that mass traces light from Mieske et al. (2013) and references therein (with the exceptions of UCD3, UCD 320, UCD 330, and M59-UCD3; Frank et al. 2011; Afanasiev et al. 2018; Voggel et al. 2018). Here stars represent the seven UCDs and two GCs for which adaptive-optics-assisted data have or will be analyzed. The colored stars represent updated stellar mass measurements after accounting for the central massive BH. Arrows illustrate the effect of the BH. The open gray star represents the M59-UCD3 estimate from Liu et al. (2015). In the case of UCD 320 and UCD 330, Voggel et al. (2018) found that their initial dynamical-to-stellar mass ratios were overestimated and did not detect a central massive BH in either object.

et al. 2018), but due to much lower S/N data (with similar spatial resolution), this BH was only detectable after assuming isotropy and fixing the stellar  $M/L$  to expected stellar population values.

In the context of the other UCDs with high BH mass fractions, it is not surprising that the BH mass in M59-UCD3 is less well determined. Using the conventional definition of the BH sphere of influence ( $r_{\text{infl}} = GM_{\text{BH}}/\sigma^2$ ), we find  $r_{\text{infl}} = 0''.03\text{--}0''.07$ , assuming  $\sigma = 65.7 \text{ km s}^{-1}$ , for M59-UCD3. Here the BH sphere-of-influence range is calculated assuming the best-fit  $M_{\text{BH}}$  for the axisymmetric Schwarzschild models and JAM models, respectively. Therefore, the BH sphere of influence for M59-UCD3 is approximately an order of magnitude less than what was found for VUCD3, M59cO, and M60-UCD1 (Seth et al. 2014; Ahn et al. 2017). Furthermore, since our adaptive optics PSF has a core FWHM of  $0''.165$  (and the diffraction limit is  $0''.07$ ), this likely explains why we cannot constrain the lower mass limit of the central BH with all three dynamical models. However, the factor of  $\sim 10$  range in BH masses in UCDs with similar stellar mass is not particularly surprising given the comparable range of BH masses seen in lower-mass (especially spiral) galaxies at a fixed dispersion or stellar mass (e.g., Kormendy & Ho 2013; Greene et al. 2016; Nguyen et al. 2017).



### 5.3. Progenitor Galaxy Properties

The combination of M59-UCD3's high luminosity and apparent BH strongly suggests that it is a tidally stripped remnant of a once more massive galaxy. We can try to estimate the progenitor mass in several ways. Assuming that UCDs follow the same  $M_{\text{BH}}$  versus bulge luminosity relation as galaxies (e.g., McConnell & Ma 2013; Mieske et al. 2013), we obtain a progenitor bulge mass of  $\sim 10^9 M_{\odot}$ . This corresponds to the total galaxy mass if we assume an early-type galaxy; in this case, the total galaxy mass would only be  $\sim 3\times$  that of the current UCD, which would make the galaxy remarkably compact, similar to M32's current size and mass. We can also estimate the mass of the NSC by assuming that it is the central two Sérsic components of the UCD (given that a King + Sérsic model provides an equally good fit; Pfeffer & Baumgardt 2013); this component has a mass of  $M_{\text{NSC}} \equiv 28 \times 10^7 M_{\odot}$  and an effective radius of  $r_{\text{eff}} = 21$  pc ( $0''.26$ ). Galaxies with similar NSCs in the Georgiev et al. (2016) sample have stellar masses between  $4 \times 10^9 M_{\odot}$  and  $10^{11} M_{\odot}$ . A similar total stellar mass range is found for galaxies with BHs between  $10^6$  and  $10^7 M_{\odot}$  in Reines & Volonteri (2015), while the  $M-\sigma$  relation implies a galaxy dispersion of  $\sim 100$  km s $^{-1}$  (e.g., Kormendy & Ho 2013). Overall, it appears likely that the original mass of M59-UCD3's progenitor was of order  $10^{10} M_{\odot}$ .

M59 has two UCDs whose progenitor galaxies' masses have been estimated to be  $\sim 10^9-10^{10} M_{\odot}$ . Therefore, we would expect the stars of these disrupted galaxies to be deposited in the outer halo of M59. Using the Sérsic fits from Kormendy et al. (2009), we calculated the total luminosity outside the projected radius of M59-UCD3 and M59cO (both  $\sim 10$  kpc), which was found to be  $L(>127'') \sim 1.2 \times 10^{10} L_{\odot}$ . Here we have assumed a constant axis ratio and position angle of  $0:7$  and  $164^{\circ}$ , respectively. We also note that Liu et al. (2015) reported a plume with similar luminosity to M59-UCD3 itself, which may be a tidal feature associated with it. Unless M59-UCD3 was remarkably compact before stripping, it appears likely that this plume, if associated with M59-UCD3, represents just a small fraction of the total amount of mass stripped off the galaxy.

### 5.4. Further Evidence and Future Prospects for SMBHs in UCDs

In this paper, we have also presented deep radio observations of three UCDs around M59 and M60, which showed a detection in only one case (around M59cO). The radio upper limits in M59-UCD3 and M60-UCD1 are lower than expected for AGN emission based on X-ray detections in these systems, although given the scatter in the fundamental plane, these measurements do not necessarily argue against an SMBH origin for the X-ray emission.












M59-UCD3 represents the fifth UCD known to host an SMBH. All UCDs with measured BH masses have been shown to have near-solar metallicities and  $\alpha$ -enhancement in the range of  $[\text{Mg}/\text{Fe}] \sim 0.1-0.5$  (Chilingarian & Mamon 2008; Francis et al. 2012; Sandoval et al. 2015; Janz et al. 2016). Both UCDs consistent with no central BH have been shown to have subsolar metallicities and solar  $[\alpha/\text{Fe}]$  ratios. This could indicate that solar- to supersolar-metallicity UCDs with alpha enhancement may serve as a secondary indicator of a central massive BH.

With current telescopes and instrumentation, our dynamical modeling effort has, thus far, been limited to either the brightest UCDs at the distance of Virgo/Fornax or some fainter UCDs at the distance of nearby large galaxies such as Centaurus A. This is due to the need to resolve the BH sphere of influence, as well as limits on the faintest sources observable with adaptive optics corrections. As the next-generation telescopes come online, such as the Extremely Large Telescope (ELT), we will be able to significantly increase the number of UCDs for which we have the capability to run dynamical models. For example, the new High Angular Resolution Monolithic Optical and Near-infrared Integral Field Spectrograph (HARMONI), which is to be mounted on ELT, has an estimated adaptive-optics-corrected angular resolution of  $0''.01-0''.03$  (Cunningham et al. 2008). Assuming two hypothetical BHs with  $M_{\text{BH}} = 10^7 M_{\odot}$  and  $M_{\text{BH}} = 10^6 M_{\odot}$  and corresponding integrated dispersions of  $\sim 50$  km s $^{-1}$  and  $\sim 30$  km s $^{-1}$ , the BH sphere of influence would be  $\sim 16$  and  $\sim 5$  pc, respectively. If we require the BH sphere of influence to be at least  $0''.05$  in size for us to resolve it with ELT/HARMONI, then we could theoretically resolve these BHs out to 19 Mpc (the distance of Fornax/Virgo) for the  $10^6 M_{\odot}$  BH and an astonishing 66 Mpc (the distance of the Perseus Cluster and many others) for the  $10^7 M_{\odot}$  BH.

C.P.A. and A.C.S. acknowledge financial support from *HST* grant GO-14067 and NSF AST-1350389. M.C. acknowledges support from a Royal Society University Research Fellowship. J.S. acknowledges support from NSF grant AST-1514763 and the Packard Foundation. A.J.R. was supported by National Science Foundation grant AST-1515084 and as a Research Corporation for Science Advancement Cottrell Scholar. R.McD is the recipient of an Australian Research Council Future Fellowship (project no. FT150100333).

*Facilities:* Gemini:Gillett (NIFS/ALTAIR), *HST* (WFC3), The National Radio Astronomy Observatory is a facility of the National Science Foundation operated under cooperative agreement by Associated Universities, Inc., These results are partially based on data obtained from the *Chandra* Data Archive.

### ORCID iDs

Christopher P. Ahn  <https://orcid.org/0000-0002-9852-2258>  
 Michele Cappellari  <https://orcid.org/0000-0002-1283-8420>  
 Jay Strader  <https://orcid.org/0000-0002-1468-9668>  
 Jonelle L. Walsh  <https://orcid.org/0000-0002-1881-5908>  
 Jean Brodie  <https://orcid.org/0000-0002-9658-8763>  
 Igor Chilingarian  <https://orcid.org/0000-0002-7924-3253>  
 Laura Chomiuk  <https://orcid.org/0000-0002-8400-3705>  
 Nadine Neumayer  <https://orcid.org/0000-0002-6922-2598>  
 Dieu D. Nguyen  <https://orcid.org/0000-0002-5678-1008>  
 Aaron J. Romanowsky  <https://orcid.org/0000-0003-2473-0369>  
 Lee Spitler  <https://orcid.org/0000-0001-5185-9876>

### References

- Afanasiev, A., Chilingarian, I., Mieske, M., et al. 2018, *MNRAS*, in press  
 Ahn, C. P., Seth, A. C., den Brok, M., et al. 2017, *ApJ*, **839**, 72  
 Arnaud, K. A. 1996, in ASP Conf. Ser. 101, *Astronomical Data Analysis Software and Systems V*, ed. G. H. Jacoby & J. Barnes (San Francisco, CA: ASP), 17  
 Bahramian, A., Heinke, C. O., Degenaar, N., et al. 2015, *MNRAS*, **452**, 3475  
 Bekki, K., Couch, W. J., & Drinkwater, M. J. 2001, *ApJL*, **552**, L105  
 Bekki, K., Couch, W. J., Drinkwater, M. J., & Shioya, Y. 2003, *MNRAS*, **344**, 399

- Boccas, M., Rigaut, F., Bec, M., et al. 2006, *Proc. SPIE*, 6272, 62723L
- Briggs, D. S. 1995, PhD thesis, The New Mexico Institute of Mining and Technology
- Brodie, J. P., Romanowsky, A. J., Strader, J., & Forbes, D. A. 2011, *AJ*, 142, 199
- Bruzual, G., & Charlot, S. 2003, *MNRAS*, 344, 1000
- Burtscher, L., Orban de Xivry, G., Davies, R. I., et al. 2015, *A&A*, 578, A47
- Cappellari, M. 2002, *MNRAS*, 333, 400
- Cappellari, M. 2008, *MNRAS*, 390, 71
- Cappellari, M. 2017, *MNRAS*, 466, 798
- Cappellari, M., Bacon, R., Bureau, M., et al. 2006, *MNRAS*, 366, 1126
- Cappellari, M., & Copin, Y. 2003, *MNRAS*, 342, 345
- Cappellari, M., & Emsellem, E. 2004, *PASP*, 116, 138
- Cappellari, M., McDermid, R. M., Bacon, R., et al. 2010, in AIP Conf. Ser. 1240, *Hunting for the Dark: The Hidden Side of Galaxy Formation*, ed. V. P. Debattista & C. C. Popescu (Melville, NY: AIP), 211
- Cappellari, M., Neumayer, N., Reunanen, J., et al. 2009, *MNRAS*, 394, 660
- Cappellari, M., Verolme, E. K., van der Marel, R. P., et al. 2002, *ApJ*, 578, 787
- Cash, W. 1979, *ApJ*, 228, 939
- Chilingarian, I. V., & Mamon, G. A. 2008, *MNRAS*, 385, L83
- Cunningham, C., Evans, C., Monnet, G., & Le Louam, M. 2008, *Proc. SPIE*, 6986, 69860K
- Dabringhausen, J., Fellhauer, M., & Kroupa, P. 2010, *MNRAS*, 403, 1054
- Dabringhausen, J., Hilker, M., & Kroupa, P. 2008, *MNRAS*, 386, 864
- Dabringhausen, J., Kroupa, P., & Baumgardt, H. 2009, *MNRAS*, 394, 1529
- Da Rocha, C., Mieske, S., Georgiev, I. Y., et al. 2011, *A&A*, 525, A86
- Drehmer, D. A., Storch-Bergmann, T., Ferrari, F., Cappellari, M., & Riffel, R. A. 2015, *MNRAS*, 450, 128
- Drinkwater, M. J., Gregg, M. D., Hilker, M., et al. 2003, *Natur*, 423, 519
- Drinkwater, M. J., Jones, J. B., Gregg, M. D., & Philipps, S. 2000, *PASA*, 17, 227
- Emsellem, E., Monnet, G., & Bacon, R. 1994, *A&A*, 285, 723
- Evtstigneeva, E. A., Drinkwater, M. J., Peng, C. Y., et al. 2008, *AJ*, 136, 461
- Evtstigneeva, E. A., Gregg, M. D., Drinkwater, M. J., & Hilker, M. 2007, *AJ*, 133, 1722
- Falcke, H., K rding, E., & Markoff, S. 2004, *A&A*, 414, 895
- Feldmeier, A., Neumayer, N., Seth, A., et al. 2014, *A&A*, 570, A2
- Feldmeier-Krause, A., Zhu, L., Neumayer, N., et al. 2017, *MNRAS*, 466, 4040
- Fellhauer, M., & Kroupa, P. 2002, *MNRAS*, 330, 642
- Fellhauer, M., & Kroupa, P. 2005, *MNRAS*, 359, 223
- Firth, P., Evtstigneeva, E. A., & Drinkwater, M. J. 2009, *MNRAS*, 394, 1801
- Forbes, D. A., Norris, M. A., Strader, J., et al. 2014, *MNRAS*, 444, 2993
- Foreman-Mackey, D., Hogg, D. W., Lang, D., & Goodman, J. 2013, *PASP*, 125, 306
- Francis, K. J., Drinkwater, M. J., Chilingarian, I. V., Bolt, A. M., & Firth, P. 2012, *MNRAS*, 425, 325
- Frank, M. J., Hilker, M., Mieske, S., et al. 2011, *MNRAS*, 414, L70
- Gebhardt, K., Richstone, D., Tremaine, S., et al. 2003, *ApJ*, 583, 92
- Gehrels, N. 1986, *ApJ*, 303, 336
- Georgiev, I. Y., B ker, T., Leigh, N., Lutzgendorf, N., & Neumayer, N. 2016, *MNRAS*, 457, 2122
- Goodman, J., & Weare, J. 2010, *Communications in Applied Mathematics and Computational Science*, 5, 65
- Gould, N. I. M., Orban, D., & Toint, P. L. 2003, *ACM Trans. Math. Softw.*, 29, 353
- Greene, J. E., Seth, A., Kim, M., et al. 2016, *ApJL*, 826, L32
- G ltekin, K., Cackett, E. M., Miller, J. M., et al. 2009, *ApJ*, 706, 404
- Haeghan, M., Jord n, A., C t , P., et al. 2005, *ApJ*, 627, 203
- Hern ndez-Garc a, L., Gonz lez-Mart n, O., Masegosa, J., & M rquez, I. 2014, *A&A*, 569, A26
- Herriot, G., Morris, S., Anthony, A., et al. 2000, *Proc. SPIE*, 4007, 115
- Hilker, M., Infante, L., Vieira, G., Kissler-Patig, M., & Richtler, T. 1999, *A&AS*, 134, 75
- Ho, L. C. 2009, *ApJ*, 699, 626
- Hou, M., & Li, Z. 2016, *ApJ*, 819, 164
- Janz, J., Forbes, D. A., Norris, M. A., et al. 2015, *MNRAS*, 449, 1716
- Janz, J., Norris, M. A., Forbes, D. A., et al. 2016, *MNRAS*, 456, 617
- Jarrett, T. H., Chester, T., Cutri, R., Schneider, S. E., & Huchra, J. P. 2003, *AJ*, 125, 525
- Kamann, S., Husser, T.-O., Dreizler, S., et al. 2018, *MNRAS*, 473, 5591
- Kimmig, B., Seth, A., Ivans, I. I., et al. 2015, *AJ*, 149, 53
- Kissler-Patig, M., Jord n, A., & Bastian, N. 2006, *A&A*, 448, 1031
- Kormendy, J., Fisher, D. B., Cornell, M. E., & Bender, R. 2009, *ApJS*, 182, 216
- Kormendy, J., & Ho, L. C. 2013, *ARA&A*, 51, 511
- Krajnovi , D., Cappellari, M., de Zeeuw, P. T., & Copin, Y. 2006, *MNRAS*, 366, 787
- Krajnovi , D., Cappellari, M., McDermid, R. M., et al. 2018, *MNRAS*, arXiv:1803.08055
- Krajnovi , D., McDermid, R. M., Cappellari, M., & Davies, R. L. 2009, *MNRAS*, 399, 1839
- Lawson, C. L., & Hanson, R. J. 1974, *Solving Least Squares Problems* (Englewood Cliffs, NJ: Prentice-Hall)
- Leung, G. Y. C., Leaman, R., van de Ven, G., et al. 2018, *MNRAS*, in press
- Liu, C., Peng, E. W., Toloba, E., et al. 2015, *ApJL*, 812, L2
- Luo, B., Fabbiano, G., Strader, J., et al. 2013, *ApJS*, 204, 14
- Maoz, D., Nagar, N. M., Falcke, H., & Wilson, A. S. 2005, *ApJ*, 625, 699
- Maraston, C. 2005, *MNRAS*, 362, 799
- Markwardt, C. B. 2009, in ASP Conf. Ser. 411, *Astronomical Data Analysis Software and Systems XVIII*, ed. D. A. Bohlender, D. Durand, & P. Dowler (San Francisco, CA: ASP), 251
- McConnell, N. J., & Ma, C.-P. 2013, *ApJ*, 764, 184
- McGregor, P. J., Hart, J., Conroy, P. G., et al. 2003, *Proc. SPIE*, 4841, 1581
- Mei, S., Blakeslee, J. P., C t , P., et al. 2007, *ApJ*, 655, 144
- Merloni, A., Heinz, S., & di Matteo, T. 2003, *MNRAS*, 345, 1057
- Mieske, S., Frank, M. J., Baumgardt, H., et al. 2013, *A&A*, 558, A14
- Mieske, S., Hilker, M., & Infante, L. 2002, *A&A*, 383, 823
- Mieske, S., Hilker, M., Jord n, A., et al. 2008, *A&A*, 487, 921
- Mieske, S., & Kroupa, P. 2008, *ApJ*, 677, 276
- Misgeld, I., & Hilker, M. 2011, *MNRAS*, 414, 3699
- Moffat, A. F. J. 1969, *A&A*, 3, 455
- Murray, N. 2009, *ApJ*, 691, 946
- Nguyen, D. D., Seth, A. C., Neumayer, N., et al. 2017, arXiv:1711.04314
- Norris, M. A., & Kannappan, S. J. 2011, *MNRAS*, 414, 739
- Norris, M. A., Kannappan, S. J., Forbes, D. A., et al. 2014, *MNRAS*, 443, 1151
- Nowak, N., Saglia, R. P., Thomas, J., et al. 2007, *MNRAS*, 379, 909
- Nowak, N., Saglia, R. P., Thomas, J., et al. 2008, *MNRAS*, 391, 1629
- Pandya, V., Mulchaey, J., & Greene, J. E. 2016, *ApJ*, 819, 162
- Peng, C. Y., Ho, L. C., Impey, C. D., & Rix, H.-W. 2002, *AJ*, 124, 266
- Pfeffer, J., & Baumgardt, H. 2013, *MNRAS*, 433, 1997
- Pfeffer, J., Griffen, B. F., Baumgardt, H., & Hilker, M. 2014, *MNRAS*, 444, 3670
- Pfeffer, J., Hilker, M., Baumgardt, H., & Griffen, B. F. 2016, *MNRAS*, 458, 2492
- Plotkin, R. M., Markoff, S., Kelly, B. C., K rding, E., & Anderson, S. F. 2012, *MNRAS*, 419, 267
- Reines, A. E., & Volonteri, M. 2015, *ApJ*, 813, 82
- Richstone, D. O., & Tremaine, S. 1988, *ApJ*, 327, 82
- Rix, H.-W., de Zeeuw, P. T., Cretton, N., van der Marel, R. P., & Carollo, C. M. 1997, *ApJ*, 488, 702
- Sandoval, M. A., Vo, R. P., Romanowsky, A. J., et al. 2015, *ApJL*, 808, L32
- Schlafly, E. F., & Finkbeiner, D. P. 2011, *ApJ*, 737, 103
- Schwarzschild, M. 1979, *ApJ*, 232, 236
- Seth, A. C. 2010, *ApJ*, 725, 670
- Seth, A. C., Cappellari, M., Neumayer, N., et al. 2010, *ApJ*, 714, 713
- Seth, A. C., van den Bosch, R., Mieske, S., et al. 2014, *Natur*, 513, 398
- Shapiro, K. L., Cappellari, M., de Zeeuw, T., et al. 2006, *MNRAS*, 370, 559
- Strader, J., Seth, A. C., Forbes, D. A., et al. 2013, *ApJL*, 775, L6
- Taylor, M. A., Puzia, T. H., Harris, G. L., et al. 2010, *ApJ*, 712, 1191
- Thomas, J., Saglia, R. P., Bender, R., et al. 2004, *MNRAS*, 353, 391
- Valluri, M., Ferrarese, L., Merritt, D., & Joseph, C. L. 2005, *ApJ*, 628, 137
- van den Bosch, R., de Zeeuw, T., Gebhardt, K., Noyola, E., & van de Ven, G. 2006, *ApJ*, 641, 852
- van den Bosch, R. C. E., & de Zeeuw, P. T. 2010, *MNRAS*, 401, 1770
- van den Bosch, R. C. E., van de Ven, G., Verolme, E. K., Cappellari, M., & de Zeeuw, P. T. 2008, *MNRAS*, 385, 647
- van der Marel, R. P., Cretton, N., de Zeeuw, P. T., & Rix, H.-W. 1998, *ApJ*, 493, 613
- Verner, D. A., Ferland, G. J., Korista, K. T., & Yakovlev, D. G. 1996, *ApJ*, 465, 487
- Verolme, E. K., Cappellari, M., Copin, Y., et al. 2002, *MNRAS*, 335, 517
- Villaume, A., Brodie, J., Conroy, C., Romanowsky, A. J., & van Dokkum, P. 2017, *ApJL*, 850, L14
- Voggel, K. T., Seth, A. C., Neumayer, N., et al. 2018, arXiv:1803.09750
- Wallace, L., & Hinkle, K. 1996, *ApJS*, 107, 312
- Wilms, J., Allen, A., & McCray, R. 2000, *ApJ*, 542, 914